AALBORG UNIVERSITY
STUDENT REPORT

Aalborg University
Studyboard for Energy

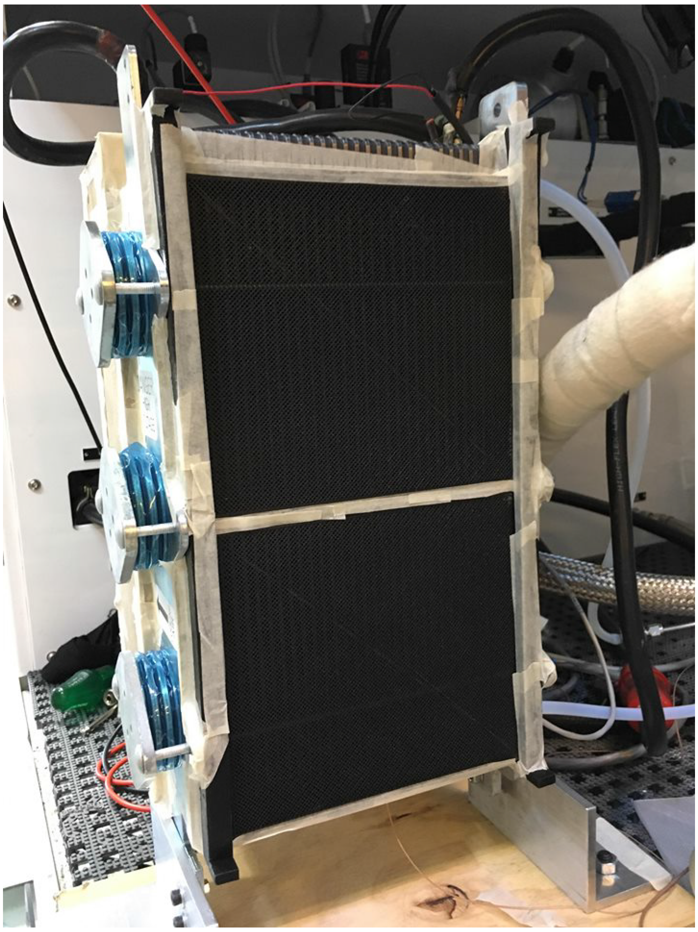

Improving the performance of an air-cooled fuel cell stack by a turbulence inducing grid

Master Thesis

Group TEPE4 - 1009

Rasheed Fallah & Line Justesen Pløger

Aalborg, Denmark

Energy Spring Semester 2018
June 1st 2018

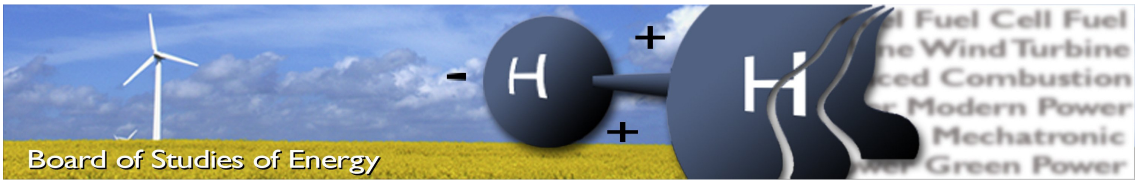

Title:
Improving the performance of an air-cooled fuel cell stack by turbulence inducing grid

Theme:
Master's Thesis

Project Period:
Spring Semester 2018

ECTS: 30 ECTS/person

Project Group:
Group TEPE4-1009

Participant(s):
Rasheed Fallah
Line Justesen Pløger

Supervisor:
Torsten Berning & Saher Al Shakhshir
Copies: 4

Page Numbers: 79
Appendix pages: vi
Supplement: None

Date of Completion:
June 1^{st} 2018

Abstract:

Proton exchange membrane fuel cells (PEMFC's) are gaining more popularity as an alternative power source for its simplicity and quick startup. They're commercialized for large number of applications ranging from automotive to stationary e.g powering telecom backup units. One of the problems regarding PEMFC's is the thermal management of the electrochemical reaction resulting in an overheat of the Ballard 1020 ACS air-cooled fuel cell stack at low current densities $0.4\,\mathrm{A/cm^2}$. Researchers in Energy Department at Aalborg University found that the biggest problem in the thermal management is the heat transfer into the air inside the cathode channels. This study aims to solve the problem by placing square and honeycomb turbulence grids before the cathode inlet. The purpose of the turbulence grids is to induce turbulences in the cathode channels and thereby increase the mixing effect in order to improve heat transfer inside the channels. A computational fluid dynamic (CFD) model is build and assisted by experimental work. The CFD results showed an an improvement of the mixing effect in the cathode channels and a reduction of the channel wall temperature is obtained. The experiments have resulted in an increase of the performance by 10.42 % and 2.75 % for the square and honeycomb grid respectively.

By signing this document, each member of the group confirms that all group members have participated in the project work, and thereby all members are collectively liable for the contents of the report. Furthermore, all group members confirm that the report does not include plagiarism.

Chapter

1

Summery

Proton exchange membrane fuel cells (PEMFC's) are electrochemical devices that convert energy of the fuel into electricity by combining hydrogen and oxygen in the absence of combustion. PEMFC's has gained more popularity as an alternative power source for its simplicity and quick startup. They're commercialized for large number of applications ranging from automotive to stationary e.g powering telecom backup units. One of the problems regarding PEMFC's is the thermal management of the electrochemical reaction resulting in an overheat of the PEMFC stack even at low current densities.

It has been found that the main problem in the thermal management is the heat transfer into the air inside the cathode channels. This study aims to solve this problem by placing a square and a honeycomb turbulence inducing grids before the cathode inlet. The purpose of the turbulence grids is to induce turbulence in the cathode channels and thereby increase the mixing effect in order to improve heat transfer inside the channels. A Computational Fluid Dynamic (CFD) model is build for only one single channel where the inlet velocity was calculated for stoichiometric flow ratio of 50 and a current density of $0.4\,\mathrm{A/cm^2}$. A constant heat flux is applied at the bottom of the channel that corresponds to the waste heat generated by the electrochemical reaction. The mixing effect will be evaluated by determining the turbulence intensity levels inside the channel. The grid is varied at different locations before the cathode channels to gain additional understanding of the mixing effects.

The model is assisted by experimental work done on both types of grids. The CFD simulation results showed an improvement of the mixing effects in the cathode channels and a reduction of the channel wall temperature is obtained. The experiments have resulted in an increasing performance by 10.42 % and 2.75 % for the square and honeycomb grid respectively. Moreover the results indicated that the turbulence grids closer to the cathode inlet decreased the average wall temperature and turbulence intensity. The highest turbulence level was achieved for the square grid at 10 mm before the cathode inlet. Overall it has been proven that the turbulence grid increases the turbulence intensity in the channel and thus increases the mixing effect in the cathode channel and thereby also increasing the performance of the Ballard 1020 ACS air-cooled fuel cell stack.

Nomenclature

Alphabetic Symbols

Symbol	Name	SI-unit
A	Area	[m^2]
c_p	Specific heat capacity	[J/kg K]
$\overrightarrow{c}$	Cell centroid	[−]
D	Grid thickness	[mm]
d	Diameter	[m]
F	Faraday constant (96.485)	[C/mol]
f	Fill Factor	[-]
G	Gibbs free energy	[J]
H	Enthalpy	[J]
HTC	Heat transfer coefficient	[W/m^2 K]
h	Heigth	[m]
I	Current	[A]
i	Current density	[A/cm^2]
L	Length	[m]
$\dot{m}$	Mass flow	[kg/s]
M	Molar mass	[kg/mol]
$\dot{n}$	Molar flow	[mole/s]
$\bar{h}$	Molar enthalpy	[J/mole]
Nu	Nusselt number	[−]]
n	Nr. of electrons per molecule	[e/mole]
p/P	pressure	[Pa]
P	Pore size	[mm]
Q	Heat	[W]
$\dot{q}$	Heat flux	[W/m^2]

Alphabetic Subscripts

Symbol	Name
amb	Ambient
an	Anode
ca	Cathode
cr	Critical
cell	Cell
el	Electrical
f	Formation
f	Fill factor
in	Inlet
out	Outlet
Ch	Channel
avg	Average
e	Equiangular
h	hydraulic
max	Maximum
MEA	Membrane assembly
min	Minimum
sat	Saturation
tot	Total
w	Wall
s	solid
grid	grid
eff	effective
ref	Reference

Alphabetic Symbols

Symbol	Name	SI-unit
R	Ideal gas constant	[atm/mol · kg]
R	Radius	[m]
Re	Reynolds number	[-]
S	Grid rod with	[mm]
S/s	Entropy	[J/K]
T	Temperature	[K]
x	Species fraction	[-]
V	Voltage	[V]
u	velocity	[m/s]
W	Power	[W]
w	Width	[m]
$u^{'}$	Fluctuating velocity	[m/s]
y^+	Dimensional distance	$[-]$
u^+	Dimensional velocity	$[-]$

Greek Symbols

Symbol	Name	SI-unit
Δ	Difference	[-]
ρ	Density	$[kg/m^3]$
ζ	Stoichiometry	[-]
μ	Dynamic viscosity	$[kg/m \cdot s]$
τ	Shear stress	$[N/m^2]$
Θ	Angle	[°]

Greek Subscripts

Symbol	Name
τ	Wall shear stress
∞	Free stream

Abbreviations

Abbreviation	**Abbreviated**
BC	Boundary Condition
CFD	Computational Fluid Dynamic
GDL	Gas Difussion Layer
HHV	Higher Heating Value
LHV	Lower Heating Value
MEA	Membrane Electrode Assembly
PEM	Proton Electrolyde Membrane
RANS	Reynolds Averaged Navier-Stokes equations
SST	Shear-Stress Transport
RH	Relative humidity

Preface

This masters thesis is written by 4^{nd} semester MSc Energy students in the period of 1^{st} February to 1^{st} of June.

The authors would like to thank their supervisors, Torsten Berning and Saher Al Shakhshir for their help and advice during the project. Furthermore the authors would like to thank Xin Gao and Chungen Yin for their help during the project.

The nomenclature with all the used symbols and subscripts can be found in the nomenclature on page V. The units related to the constants or variables are also listed here. The abbreviations are written in full the first time, afterwards the abbreviation will be used. The abbreviations can be found on page VII.

The chapters are numbered with Arabic numbers, and section and subsection numbers follows after one or two full stops respectively. Each figure, table or equation are numbered in the same way, first chapter number and then the number of each type afterwards, sub-figures have the additional Latin letter. A list of figures and tables can be found in the appendices on page i and iv respectively.

Citations are given in square brackets with name(s) (including company name(s)) and year, e.g. [Roach, 1987]. If the name(s) of the author(s) are gives in the text the year will be printed in square brackets just behind, e.g. Roach [1987]. The bibliography are given in the end of the appendices starting on page v.

Contents

CHAPTER

2 Introduction

2.1 Historical Review of PEM Fuel Cell

Fuel cell technology is an old invention and was discovered by Sir William Grove in 1839. In the following century, various unsuccessful attempts on creating an operative fuel cell was carried out [Barbir, 2013].

As is shown in figure 2.1 the fuel cell was reinvented in 1939 where Francis T. Bacon started his work on fuel cells. In the late 1950's, he succeeded in making a 6 kW fuel cell stack. The first practical use of fuel cells was the Gemini program in the early 1960s, under the U. S. space program, the fuel cell was developed by General Electric, and was the first Proton exchange membrane fuel cell [Barbir, 2013].

Hereafter fuel cells were used in the Apollo space project as well. During the 1960s different companies experimented with non space applications for fuel cells. One example is the fuel cell driven van made by General Motors. Afterwards fuel cells was almost forgotten in all terrestrial applications until the early 1990s. In the early 1990s fuel cells were successfully applied in different applications. One of these was a passenger car in 1993 made by Energy Partners the car was running on PEM fuel cells. This gave rise to an increasing interest

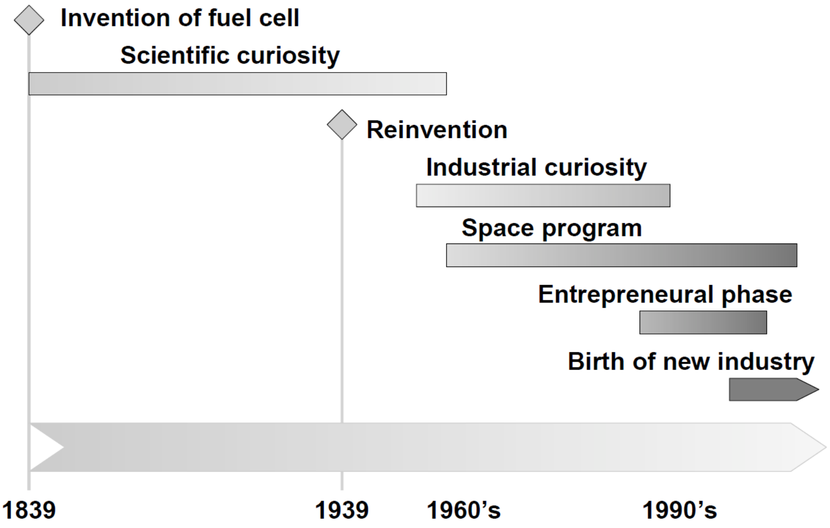

Figure 2.1. Time line of fuel cells [Barbir, 2013]

in fuel cells and by the end of the 1990s every manufacturer of cars had given fuel cell powered a go [Barbir, 2013].

Today fuel cells are still a very interesting subject due to the fact that it is a zero emission technology that generates electricity. Fuel cell converts chemical energy into DC current, and is thereby categorized as an electrochemical energy converter [Barbir, 2013].

2.2 Fuel cell working principle

Proton electrolyte membrane (PEM) is a popular technology because of its simplicity and quick start-up. At the heart of a PEM fuel cell is the membrane electrode assembly (MEA). The MEA is squeezed between two flow field plates that are mirrored to make bipolar plates when the cells are stacked in series for greater voltage purpose. MEA consist of a PEM, gas diffusion layers (GDL) and catalyst layers, see figure 2.2.

The PEM is impermeable to gasses but conducts protons. The GDL acts as porous electrode that is made of carbon cloth or carbon fiber paper [Barbir, 2013]. GDL facilitates diffusion of reactants across the catalyst layered membrane. The surface area and porosity of GDL allows the reactants in the channels of flow field plates to diffuse along the active area (catalyst area) of the membrane [Fuel Cells Etc, 2013]. The catalyst layers are typically platinum coated in carbon and are indirect contact with with GDL and PEM. The electrochemical reaction takes place at the interface between the membrane and catalyst layers [Barbir, 2013].

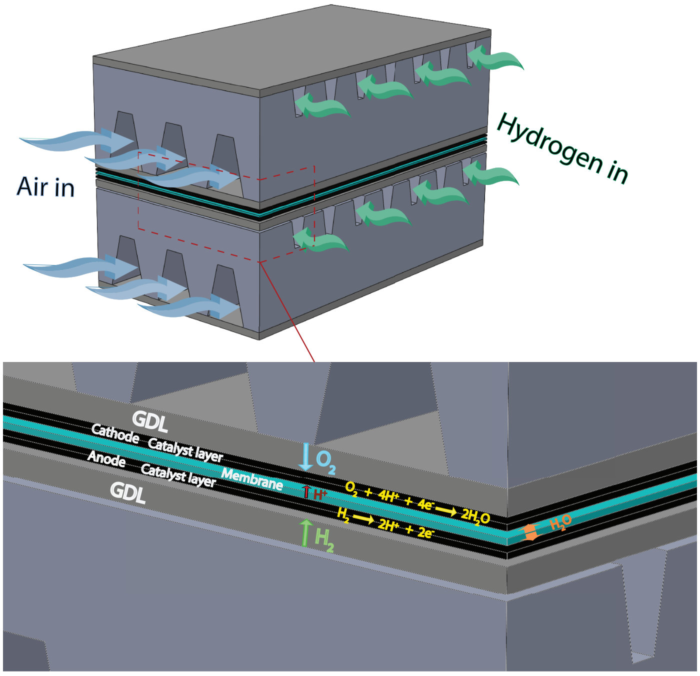

Figure 2.2. Schematic of air and hydrogen supply in a PEM fuel cell.

Hydrogen, H_2, is supplied at the porous anode side, where it is split into positively charged hydrogen protons (H^+) and negatively charged electrons (e^-). The membrane allows the hydrogen protons to travel to the cathode side whereas the electrons are transported through an external circuit to produce electrical power.

At the porous cathode side air is supplied and the electrons interact with oxygen supply forming O_2^-. This oxide then reacts with the hydrogen ions and forming water H_2O. The reactions in a PEM fuel cell at the cathode and anode can also be formulated as following [Barbir, 2013]:

$$\text{Anode side} \qquad H_2 \rightarrow 2H^+ + 2e^- \tag{2.1}$$

$$\text{Cathode side} \qquad \frac{1}{2}O_2 + 2H^+ + 2e^- \rightarrow H_2O \tag{2.2}$$

$$\text{Overall reaction} \qquad H_2 + \frac{1}{2}O_2 \rightarrow H_2O \tag{2.3}$$

These three basic reactions accurately describes the main process in a fuel cell.

2.3 Voltage Losses

An open circuit potential implies that a fuel cell is supplied with reactant gases, but the electrical circuit is not closed and thus it will not generate any current. However the open circuit potential would be close to the theoretical cell potential if not it was because of the losses, even when no external current is generated. The open circuit potential is significantly lower than the theoretical potential, usually less than 1 V [Barbir, 2013]. If the electrical circuit is closed with a load the electrical potential is expected to drop even further as a function of current being generated due to losses. There are different kinds of voltage losses caused by following:

- Activation losses.
- Ohmic resistance losses.
- Mass transport losses (concentration losses).

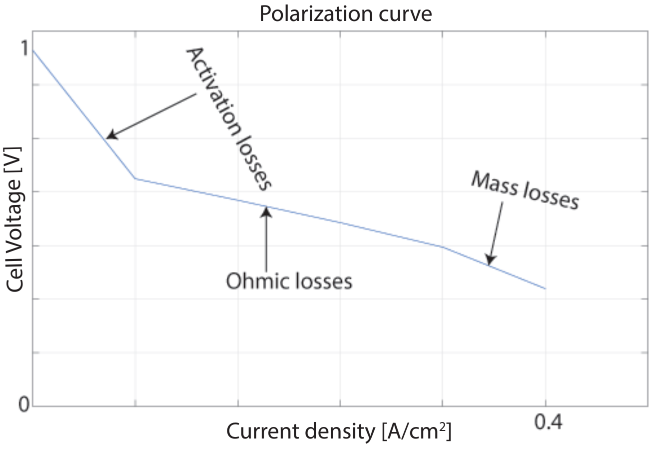

Figure 2.3. Sketch of variation of cell voltage with current density and corresponding losses.

2.3.1 Activation losses

Activation losses are caused by the slow reaction kinetics (of oxygen reduction) on the surface of the electrodes . The rapid voltage decrease is due to electrochemical reaction, see figure 2.3. The activation losses are the main cause of voltage drop [Kaur, 2016].

2.3.2 Ohmic losses

The ohmic losses occur due to resistance of the flow of ions in the electrolyte and electrons at the cathode through the electrically conductive fuel cell components [Barbir, 2013]. The corresponding voltage drop is linearly proportional to the current density which can also be seen in figure 2.3

2.3.3 Mass transport losses

The concentrations losses also known as gas transport losses occurs when a reactant is rapidly consumed at the electrode by the electrochemical reaction such that the concentrations gradient is established [Barbir, 2013]. Hydrogen and oxygen are fed on the anode and cathode respectively. During fuel cell operation the concentration of oxygen and hydrogen decreases on the cathode and anode respectively. The decrease in concentration depends on the circulation of of air and hydrogen around the cathode and anode and the current being drawn from the fuel cell. As the partial pressure of oxygen and hydrogen changes the concentrations i.e. the decrease in concentration causes a decrease in partial pressure and thus the decrease in partial pressure leads to a decrease in cell voltage [Kaur, 2016].

2.4 Investigated Fuel Cell

The fuel cell stack utilized in this study is a Ballard power systems air-cooled stack Mark1020 ACS. A 3D CAD drawing of the fuel cell stack is shown in figure 2.4. The fuel cell stack consist of 28 cells stacked in series that makes a total stack height of 103 mm, total width of 351 mm and total length of 55.4 mm, see table 2.1. Each cell has a channel for hydrogen supply and air supply respectively.

Table 2.1. Stack dimensions and specifications

	Dimensions and specifications	
Stack length, L_{stack}	55.4	[mm]
Stack height, h_{stack}	103	[mm]
Stack width, w_{stack}	351	[mm]
Working current range, I	0 - 87	[A]
Optimal operating temperature, T_{opt}	42 - 66	[°C]

The working current range for at new and fully conditioned Mark1020 ACS stack is 0 A to 87 A but the recommended maximum current is 75 A. The optimal temperature range

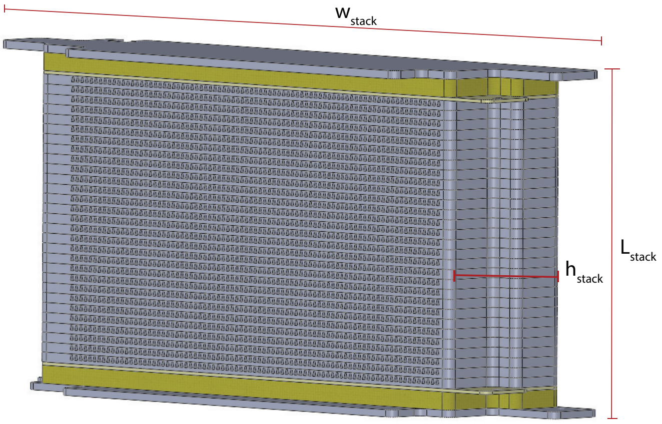

Figure 2.4. 3D drawing of the air-cooled fuel cell stack.

of Mark1020 ACS stack varies with stack current, from 42 °C at 7.5 A to about 66 °C at 78 A.

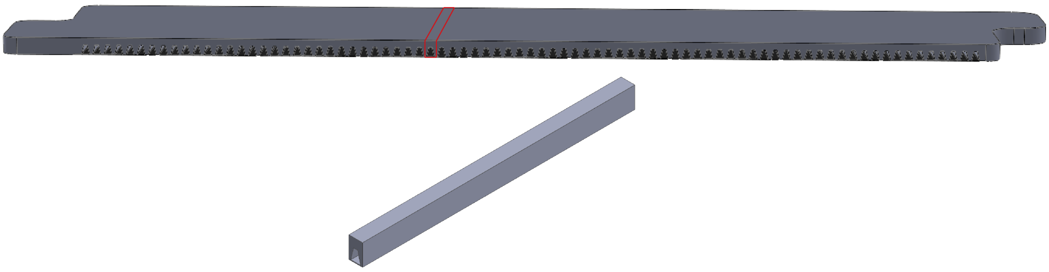

Figure 2.5. 3D drawing of a single fuel cell and single air channel.

One single cell consist of 81 air channels and at the cathode sideeach channel is trapezoid-formed as depicted in figure 2.5.

CHAPTER

3 Fuel Cell Thermodynamics

In this chapter the thermodynamics of the fuel cell will be presented based on the first law of thermodynamics, assuming ideal gas behavior and neglecting changes in potential and kinetic energy. Furthermore analysis will be carried out to determine the flow rates of the air and the corresponding flow velocities of the air to attain a desired fuel cell operating temperature.

3.1 Molar Inlet Streams

In order to apply the first law of thermodynamics in PEM fuel cell, the molar flow rates will be formulated before calculating the enthalpy streams. The incoming molar stream of oxygen is given as [Berning and Kær, 2018]:

$$\dot{n}_{O2,in} = \zeta_{ca} \frac{I}{4F} \tag{3.1}$$

where ζ_{ca} is the cathode stoichiometric flow ratio and F is Faraday constant 96.485 Coulombs/electron · mol. The incoming molar stream of nitrogen is:

$$\dot{n}_{N2,in} = \frac{79}{21}\dot{n}_{O2,in} = 3.7619 \cdot \zeta_{ca} \cdot \frac{I}{4F} \tag{3.2}$$

A certain amount of water vapor is entering the cell which depends on the inlet relative humidity RH_{in} of the ambient air and is considered as a free parameter:

$$RH_{in} = \frac{p_{H2O}}{p_{sat}(T)} = x_{H2O}\frac{p_{amb}}{p_{sat}(T)} = \frac{\dot{n}_{H2O,in}}{\dot{n}_{tot,in}}\frac{p_{amb}}{p_{sat}(T)} \tag{3.3}$$

Solving for $\dot{n}_{H2O}$ gives:

$$\dot{n}_{H2O,in} = RH_{in} \cdot \frac{p_{sat}(T)}{p_{amb}} \cdot \dot{n}_{tot,in} = RH_{in} \cdot \frac{p_{sat}(T)}{p_{amb}} \left(\dot{n}_{H2O,in} + \dot{n}_{O2,in} + \dot{n}_{N2,in}\right) \tag{3.4}$$

which then results in:

$$\dot{n}_{H2O,in} = RH_{in} \cdot \left(\frac{p_{sat}(T)}{p_{amb}} - RH_{in}\right)^{-1} \cdot \left(\dot{n}_{O2,in} + \dot{n}_{N2,in}\right) \tag{3.5}$$

Similar to nitrogen and oxygen molar streams, it is preferable to express the amount of water entering the cell as a function of the current and stoichiometry. Substituting for molar streams of oxygen and nitrogen in eq. 3.1 and 3.2 respectively, eq. 3.5 yields [Berning and Kær, 2018]:

$$\dot{n}_{H2O,in} = RH_{in} \cdot \left(\frac{p_{sat}(T)}{p_{amb}} - RH_{in} \right)^{-1} \cdot 4.7619 \cdot \zeta_{ca} \frac{I}{4F} \cdot \tag{3.6}$$

The saturation pressure p_{sat} is a function of temperature only and can be expressed by Antoine's equation [Berning and Kær, 2018]:

$$p_{sat}\left(T\right) = D \cdot e^{\left(A - \frac{B}{C+T}\right)} \tag{3.7}$$

where A=8.07131, B=1730.63, C=233.426 and D are coefficients that converts the unit $mmHg$ into Pa that is 133.233. At ambient temperature the saturation pressure is 3158 Pa.

It is assumed that dry hydrogen is entering the cell at the anode side with a specified stoichiometric flow ratio:

$$\dot{n}_{H2,in} = \zeta_{an} \cdot \frac{I}{2F} \tag{3.8}$$

3.2 Molar Outlet Streams

For molar outlet streams that is leaving the cell, for O_2 it is:

$$\dot{n}_{O2,out} = (\zeta_{ca} - 1) \cdot \frac{I}{4F} \tag{3.9}$$

For nitrogen it is given as:

$$\dot{n}_{N2,out} = \dot{n}_{N2,in} = 3.7619 \cdot \zeta_{ca} \cdot \frac{I}{4F} \tag{3.10}$$

Water at the outlet is the amount that has entered the cell plus the product water. It is assumed that all the product water leaves at the cathode side resulting in the very low anode side stoichiometric flow ratios and thus the molar stream of water becomes [Berning and Kær, 2018]:

$$\dot{n}_{H2O,out} = \dot{n}_{H2O,in} + \frac{I}{2F} = RH \cdot \left(\frac{p_{sat}}{p_{amb}} - RH \right)^{-1} \cdot 4.7619 \cdot \zeta_{ca} \cdot \frac{I}{4F} + \frac{I}{2F} \tag{3.11}$$

3.3 Energy Balance

The energy balance of the fuel cell is conducted by applying the first law of thermodynamics where the sum of all energy inputs must equal the sum of all energy outputs, thus the energy balance can be written as following [Barbir, 2013]:

$$\sum \left(H_i\right)_{in} = W_{el} + \sum \left(H_i\right)_{out} + Q \tag{3.12}$$

where W is the amount of work that is extracted from the cell. The system is considered to be adiabatic and thus $Q = 0$. W is in this case electrical work which is given as:

$$W_{el} = V_{cell} \cdot I_{cell} \tag{3.13}$$

where V_{cell} is the average cell voltage and I_{cell} is the cell current. Assuming ideal gas behaviour the enthalpy streams are expressed as following [Berning and Kær, 2018]:

$$H = \sum \dot{n}_i \bar{h}_i = \sum \dot{n}_i \left\lfloor \bar{h}_f^0 + \left(\bar{h} - \bar{h}^0\right) \right\rfloor = \sum \dot{n}_i \left\lfloor \bar{h}_f^0 + \bar{c}_p \left(T - T^0\right) \right\rfloor \tag{3.14}$$

where $\bar{h}$ is molar enthalpy given in $[J/mole]$, $\bar{h}_f^0$ is the enthalpy of formation. The molar enthalpy of any species consists of two terms, namely the enthalpy of formation at 25 °C and 1 atm and the sensible enthalpy due to temperature increase.

In order to calculate the adiabatic gas outlet temperatures, the first-law of thermodynamic reduces to:

$$W = \sum \dot{n}_{i,out} \bar{h}_{i,out} - \sum \dot{n}_{i,in} \bar{h}_{i,in} \tag{3.15}$$

It is assumed that the incoming air is at the standard conditions of 25 °C and 1 atm such that the incoming enthalpy streams of nitrogen, oxygen and hydrogen are zero compared to the standard conditions, see table 3.2. The gas properties at standard condition is given in table 3.1.

Table 3.1. Gas properties at standard condition

	M $(kgmol^{-1})$	c_p $(kJkmol^{-1}K^{-1})$	h^0 $(kJmol^{-1})$
Hydrogen, H_2	2	28.614	8468
Oxygen, O_2	32	30.00	8682
Nitrogen, H_2	28	29.484	8669
Water (vapor) H_2O (g)	18	33.462	9904

Inserting the above expression into the energy balance equation it then becomes [Berning and Kær, 2018]:

$$\begin{aligned} V_{cell} \cdot I_{cell} =& \dot{n}_{O2,out}\left(h - h^0\right)_{02} + \dot{n}_{N2,out}\left(h - h^0\right)_{N2} + \dot{n}_{H2,out}\left(h - h^0\right)_{H2} \\ +& \quad \dot{n}_{H2O,out}\left(h_f^0 + h - h^0\right)_{H2O} \end{aligned} \tag{3.16}$$

The enthalpy of formation is only considered for the water. The product water will be in gas phase and it is assumed for simplicity that the incoming air is completely dry such that no water vapor is entering.

It is seen from eq. 3.1, 3.2 and 3.5 that the molar flow rates depend directly on the cell current which indicates that it can be cancelled out in eq 3.16. Inserting the molar flow rates in eq. 3.16 and cancelling the cell current, the equation can thus be expressed as[Berning and Kær, 2018]:

$$\begin{aligned} V_{cell} =& \frac{1}{4F} \cdot (\zeta_{ca} - 1) \cdot \left(\bar{h}_{O2}\left(T_{out}\right) - 8682 \frac{kJ}{kmole}\right) \\ &+ \frac{1}{4F} \cdot 3.762 \cdot \zeta_{ca} \cdot \left(\bar{h}_{N2}\left(T_{out}\right) - 8669 \frac{kJ}{kmole}\right) \\ &+ \frac{1}{2F} \cdot (\zeta_{ca} - 1) \cdot \left(\bar{h}_{H2}\left(T_{out}\right) - 8468 \frac{kJ}{kmole}\right) \\ &+ \left[\frac{RH \cdot \frac{p_{sat}(T)}{p_{tot}}}{\left(1 - RH \cdot \frac{p_{sat}(T)}{p_{tot}}\right)} \cdot 4.762 \cdot \frac{\zeta_{ca}}{4F} + \frac{1}{2F}\right] \\ &\left(-241.820 \frac{kJ}{kmole} + \bar{h}_{H2O}\left(T_{out}\right) - 8468 \frac{kJ}{kmole}\right) \end{aligned} \tag{3.17}$$

Eq. 3.17 is applied to study the adiabatic cell temperature at different stoichiometric flow ratios which is seen in figure 3.1 at different cathode stoichiometric flow ratios. The stoichiometric flow ratio is fixed at the anode side which is 1.1 and the operating conditions are at an inlet temperature of 25 °C with a relative humidity of 30%.

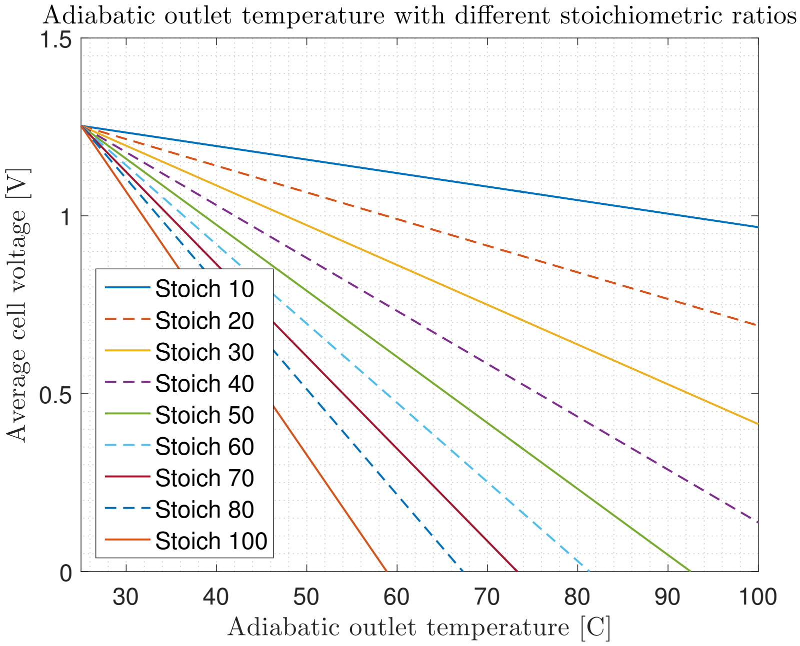

Figure 3.1. Shows the dependency of the adiabatic outlet temperature of outlet gases on the operating cell voltage. The operating inlet conditions were with a temperature of 25 °C and a relative humidity of 30% with dry hydrogen at the anode side and at a fixed stoichiometric flow ratio of 1.1 [Berning and Kær, 2018].

The cell voltage in figure 3.1 decreases for a given stoichiometric flow ratio which results in production of more waste heat and therefore the cathode outlet temperature increases. Thus additionally to the cell voltage, the cathode stoichiometric flow ratio is the most important parameter. Furthermore the ambient temperature and the relative humidity also has an impact on the adiabatic outlet temperature.

3.4 Heat Generation in PEM Fuel Cell

In this section the heat generation of PEM fuel cell in a channel will be estimated for later simulation purpose.

3.4.1 Heat of Reaction

The overall reaction in the fuel cell is given by [Barbir, 2013]:

$$H_2 + \frac{1}{2}O_2 \rightarrow H_2O \tag{3.18}$$

this reaction may have several intermediate steps but for now this reaction accurately describes the main process in the fuel cell. The reaction is the same as the reaction of hydrogen combustion which is an exothermic process. The exothermic process means that energy is released in the process:

$$H_2 + \frac{1}{2}O_2 \rightarrow H_2O + heat \tag{3.19}$$

The heat or enthalpy of a chemical reaction is the difference between the heats of formation h_f of products and reactants. For 3.19 this means that:

$$\Delta H = (h_f)_{H_2O} - (h_f)_{H_2} - \frac{1}{2}(h_f)_{O_2} \tag{3.20}$$

Heat of formation of water at 25 °C is −286 KJ/mol and heat of formation of elements is zero, thus eq. 3.19 becomes [Barbir, 2013]:

$$\Delta H = (h_f)_{H_2O} - (h_f)_{H_2} - \frac{1}{2}(h_f)_{O_2} = -286\frac{kJ}{g} - 0 - 0 = -286\frac{kJ}{mol} \tag{3.21}$$

$$H_2 + \frac{1}{2}O_2 \rightarrow H_2O\,(l) + 286\frac{kJ}{mol} \tag{3.22}$$

The positive sign in eq. 3.22 indicates that heat is the product of the reaction. The equation is only valid at 25 °C and atmospheric pressure where water is in liquid form. The enthalpy in eq. 3.22 is called hydrogen heating value. It is the amount of heat that has been generated by a complete combustion of 1 mol of hydrogen. If 1 mol hydrogen is ignited and fully combusted with $\frac{1}{2}$ mol of oxygen enclosed in a calorimetric bomb and allowed to cool down to 25 °C at atmospheric pressure, then there will only be liquid water left in the combustion which should show that 286 kJ/mol of heat was released. This is known as hydrogen higher heating value (HHV). If hydrogen is combusted with sufficient excess of air and allowed to cool down to 25 °C then the product water will be in the form of vapor mixed with un-burned oxygen and thus less heat will be released, only 241 kJ/mol which is known as hydrogen's lower heating values (LHV) [Barbir, 2013].

3.4.2 Theoretical Fuel Cell Potential

In the chemical reaction of hydrogen, entropy is produced due to the reaction and because of that some portion of hydrogen's HHV cannot be converted into useful work or electricity in case of fuel cell. The ideal amount of hydrogen's HHV that can be converted into electricity in a fuel cell corresponds to Gibbs free energy which is given as the following [Barbir, 2013]:

$$\Delta G = \Delta H - T\Delta S \tag{3.23}$$

where ΔS is entropy. Similar to ΔH, ΔS is the difference between entropies of products and reactants:

$$\Delta S = (s_f)_{H2O} - (s_f)_{H2} - \frac{1}{2}(s_f)_{O2} \tag{3.24}$$

where s_f is the entropy of formation. The theoretical potential of fuel cell is given by:

$$E = \frac{\Delta G}{nF} \tag{3.25}$$

where F is Faradays constant and n is number of electrons per molecule.

Table 3.2. Enthalpy and entropy of formation [Barbir, 2013]

	h_f $(kJ\ mol^{-1})$	s_f $(kJ\ \ mol^{-1}\ K^{-1})$
Hydrogen, H_2	0	0.13066
Oxygen, O_2	0	0.20517
Water, H_2O (l)	-286.02	0.06996
Water (vapor) H_2O (g)	-241.98	0.18884

Knowing the values of h_f and s_f in table 3.2 at ambient temperature of 25 °C and atmospheric pressure, the theoretical cell potential is calculated to be [Barbir, 2013]:

$$E = \frac{-\Delta G}{nF} = \frac{237.340}{2 \cdot 96.485}\frac{Jmol^{-1}}{Asmol^{-1}} = 1.23 \quad Volts \tag{3.26}$$

3.4.3 Waste Heat Generation

The heat generated in the fuel cell is given as [Barbir, 2013]:

$$Q = (1.254 - V_{cell}) \cdot I \cdot n_{cell} \tag{3.27}$$

where I is the stack current and n_{cell} is the number of cells in the PEM fuel cell stack. It is required that the product water is in the gaseous form at the cathode side and therefore LHV value of 33.3 kWh/kg corresponding to an electrolyzer voltage of 1.254 V [HP] is used in eq. 3.27. This value is for a system that combines hydrogen and oxygen and produces gaseous water rather than liquid water.

Eq. 3.27 is the heat generation based on number of cells and stack current. As in this project only a channel will be used in the simulations, eq. 3.27 becomes:

$$Q = (1.254 - V_{cell}) \cdot i \tag{3.28}$$

where i is current density. With a current density of 0.385 A/cm^2 and cell voltage of 0.582 V the waste heat generated becomes 0.2587 W/cm^2 which is 2587 W/m^2.

3.5 Polarization Curve and Adiabatic Outlet Temperature

Mark1020 ACS air cooled fuel cell stack can maximum operate at a current density of 0.385 A/cm^2. Figure 3.2 shows the polarization curve of the PEM fuel cell at the beginning of life time and end of life time.

It is seen that the maximum current density at the beginning of life time is 0.385 A/cm^2 while at the end of life time it is 0.25 A/cm^2. The corresponding maximum power density at the beginning of life time is 0.224 W/cm^2 and 0.13 W/cm^2 at the end of life time.

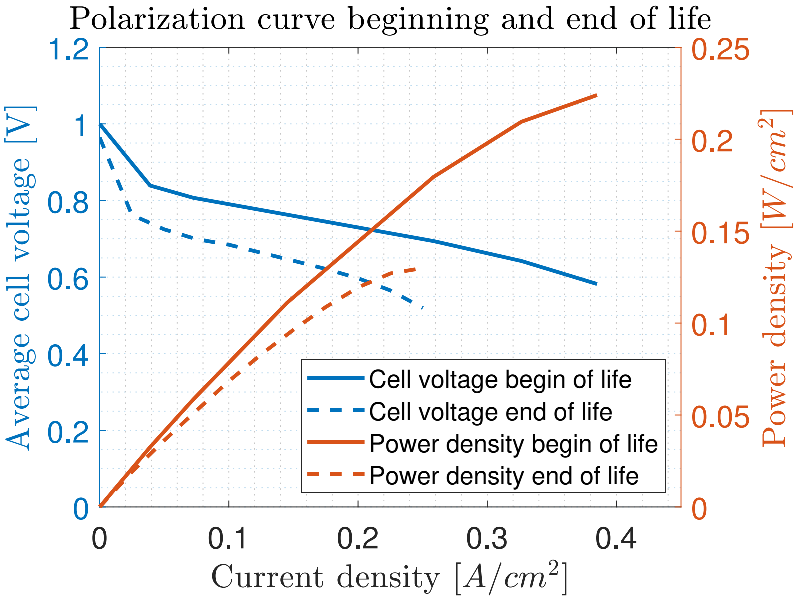

Figure 3.2. A graph of cell voltage and power density as a function of current density at the beginning of life time and end of life time.

It is highly desirable to operate at higher current densities which leads to higher power densities. In order to operate at higher current densities an effective cooling method needs to be applied to the fuel cell stack. In this project forced air cooling method system is incorporated in order to make the cooling more effective. A promising solution to increase the power density and further making the cooling more effective, a turbulence inducing grid will be incorporated in the cooling system [Torsten Berning and Shakhshir, 2018]. This turbulence inducing grid will be placed before the cathode inlet in order to create turbulences. For effective cooling method a correct air flow needs to be determined. As simulations is done with only one channel a proper inlet velocity must be calculated. This will be introduced in the next section.

3.6 Inlet Channel Velocity

In this section the calculation of the inlet velocity of air in PEM fuel cell channel will be introduced.

In order to determine the inlet velocity at the cathode, the corresponding formula needs to be derived. First the velocity must be found from the equation of mass flow rate in a duct:

$$u = \frac{\dot{m}}{\rho \cdot A_{ch}} \tag{3.29}$$

where A_{ch} is the channel cross sectional area. From ideal gas equation density can be found as [Barbir, 2013]:

$$\rho = \frac{M_{air} \cdot P}{R \cdot T} \tag{3.30}$$

where M_{air} is the molar mass of air and R is the ideal gas constant R=0.0821 atm · /mol · K. The mass flow rate of air is expressed by following equation:

$$\dot{m}_{air} = \frac{1}{x_{O_2}, in} \cdot M_{O_2} \tag{3.31}$$

where $x_{O_2,in}$ is the molar fraction of the reactants O_2 and H_2 of the incoming humid gasses. The molar fraction of the water vapor $x_{H_2O,in}$ in the incoming gas stream is the ratio of the saturation pressure and the total pressure:

$$x_{H_2O,in} = \frac{p_{sat}}{p_{in}} \tag{3.32}$$

As the ratio of nitrogen and oxygen in dry air is known to be 79:21, the inlet oxygen fraction can be found by:

$$x_{O_2,in} = \frac{1 - x_{H_2O,in}}{1 + \frac{79}{21}} \tag{3.33}$$

The oxygen mass flow rate can be determined by following equation [Barbir, 2013]:

$$\dot{m}_{O_2} = \zeta \frac{I}{4 \cdot F} \cdot M_{O_2} \tag{3.34}$$

The current is a product of current density and the cell active area, thus equation 3.34 becomes:

$$\dot{m}_{O_2} = \zeta \frac{i}{4 \cdot F} \cdot M_{O_2} \cdot A_{MEA} \tag{3.35}$$

Substituting for density and mass flow rate in equation 3.29, the equation for the velocity at the cathode inlet becomes:

$$u_{in} = \zeta \frac{i}{4 \cdot F} \cdot A_{MEA} \frac{1}{x_{O_2,in}} \frac{R \cdot T_{in,ca}}{p_{in}} \frac{1}{A_{ch}} \tag{3.36}$$

Only half the channel cross sectional area A_{ch} and half the geometrical area of the membrane A_{MEA} are considered in the calculation. The A_{ch} and A_{MEA} are depicted in figure 3.3.

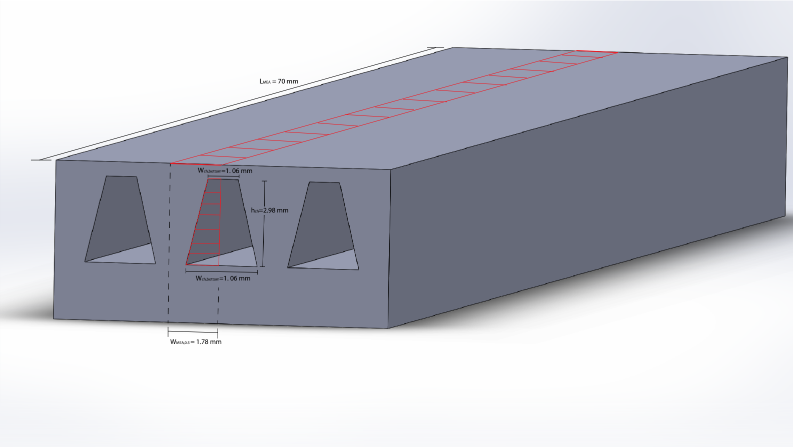

Figure 3.3. Sketch of the half channel cross sectional area and half the geometrical area of the membrane which is included in the calculation.

Knowing all the values in eq. 3.36 which is given in table 3.3, the inlet velocity is calculated to be 2.81 m/s.

Table 3.3. Pre-determined parameters.

Inlet temperature, T_{in}	298.15	[K]
Inlet pressure, P	101.325	[kPa]
Saturation pressure of water at 25 °C	3.16	[kPa]
Geometrical area of the membrane, A_{MEA}	124.60	$[mm^2]$
Cross sectional area of the channel, A_{ch}	2.652	$[mm^2]$
Stoichiometry, ς	50	[-]
Number of electrones per mole of reactants	4	[-]
Current density, i	0.385	$[A_{cm^2}]$

The corresponding Reynolds number Re, is calculated [Munson et al., 2012]:

$$Re = \frac{\rho \cdot d_h \cdot u_{in}}{\mu} \tag{3.37}$$

where d_h is the hydraulic diameter, ρ is the density of air and μ is the dynamic viscosity. The hydraulic radius for a trapezoid is calculated as the following [PRITCHARD, 2016]:

$$R_h = \frac{\left(h_{ch} \cdot \frac{w_{ch,top}+w_{ch,bottom}}{2}\right)}{\left(w_{ch,top} + 2 \cdot \left(\left(\frac{w_{ch,bottom}-w_{ch,top}}{2}\right)^2 + h_{ch}^2\right)^{\frac{1}{2}}\right)} \tag{3.38}$$

thus the hydraulic diameter becomes:

$$d_h = R_h \cdot 2 \tag{3.39}$$

Knowing all the dimensions of the cross sectional area of the channel, the corresponding Re number is calculated to be $Re = 265$.

3.6.1 Free Stream Velocity

The free stream velocity is calculated based on the area ratios.

$$\rho_1 u_1 A_1 = \rho_2 u_2 A_2, \quad \rho = constant \tag{3.40}$$

$$u_1 A_1 = u_2 A_2 \tag{3.41}$$

$$u_\infty A_\infty = u_{in} A_{ch} \tag{3.42}$$

The free stream area A_∞ is measured to be 5 cm × 5 cm in the center of the PEM fuel cell stack, see figure 3.4.

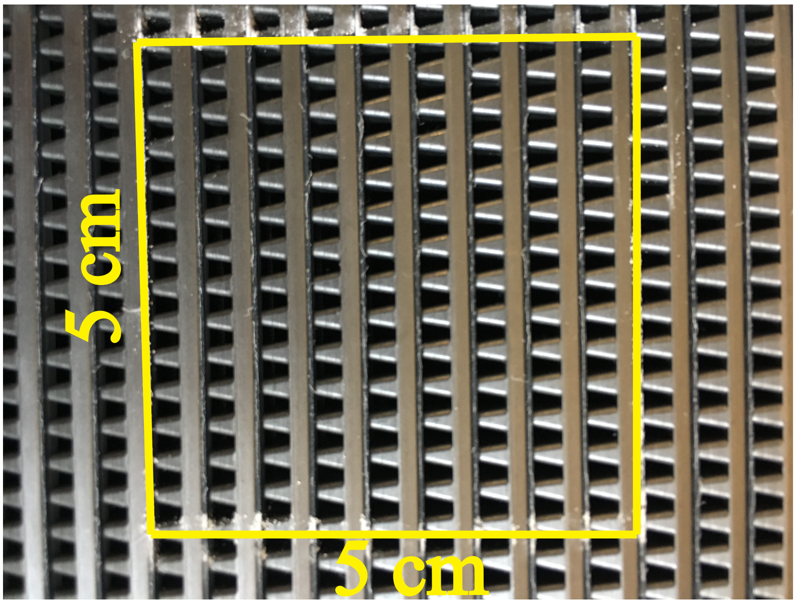

Figure 3.4. Free stream area is 5 cm × 5 cm with 126 channels.

The number of channels in that area is counted to be 126 and then multiplied by the cross sectional area of one channel in order to get the total cross sectional area of channels in that 5 cm × 5 cm area. Thus solving eq. 3.42 for free stream velocity u_∞ the free stream velocity becomes 0.7485 m/s, which for the modelling purposes til be rounded to 0.75 m/s.

CHAPTER

4

Problem statement

This chapter will outline the objective of this project.

The main objective of this project is to model the air-cooled PEM fuel cell stack with one channel and design a turbulence grid. The aim of the grid is to induce turbulence by disturbing channel boundary layer and thereby introduce more effective cooling. The grid will be positioned in front of the channel at different distances. The modelling and simulations will be conducted with the available CFD package (ANSYS FLUENT). Experiments will be conducted in order to validate the CFD simulations. The project will henceforth be written to answer the following problem statement:

What are the effects of turbulence grid on the performance of air-cooled PEM fuel cell stack and how should it be modelled in order to capture the turbulences?

To make a platform for solving the problem, the following research questions will be answered to, throughout this report.

- How can the CFD simulations be verified?
- Which effect does grid distance before the cathode inlet affect the performance?
- Does the grid increase the turbulence?
- How does turbulence grid effects the Nu number throughout the channel and the entry region?

The evaluating parameter in the model will be temperature and Nusselt number. As the CFD simulations will be conducted with and without the grid placed in front of the channel, the evaluation of the temperature and Nusselt number will outline the effects of the turbulence grid. From this it will also be investigated what is the optimal position of the turbulence grid before the channel.

The experiments will be conducted in order to evaluate the current density and temperature in the air-cooled PEM fuel cell stack. The temperature will be compared to the CFD model.

CHAPTER

5

Turbulence Grid

Turbulence grids have been widely used in wind tunnel test sections in order to introduce disturbances and generate turbulences. Paradoxically, they are also used to eliminate turbulences or pressure nonuniformities. The effect of turbulence grid can be categorized into two parts: a manipulation effect and a wake effect [Roach, 1987]. The manipulation effect is a process where the spectrum of the turbulence is either altered, reducing or increasing the effect of the upstream turbulent eddies. The wake effect is a process, which contributes turbulent energy to the downstream flow field. This energy consist of high frequency, and as results tend to decrease the scale of the upstream turbulent eddies. The turbulent energy generated is found to decay rapidly and the eddy scales increase in size with downstream flow field. Furthermore the level of turbulence energy generated in the grid is directly proportional to the pressure loss through the grid [Roach, 1987].

Mikhailova et al. [2005] conducted experimental work on investigation of the effect of the Re number on the degeneration law for turbulence generated grid by studying parameters such as fill factor f, grid hydraulic diameter $d_{h,grid}$, based on the rod diameter and velocity u_{grid}. According to the article the critical Re_{Cr} number for a grid to induce turbulences is $Re_{cr} \approx 175$. Furthermore, the investigation showed that generation of turbulence primary depends on the fill factor and Re number.

Turbulence grids in this study are designed based on Re_{Cr}, studied by Mikhailova et al. [2005]. Two grids have been designed and 3D printed. The first grid is made of square pores inclined with and angle of 45°. The grid has a thickness D of 1 mm with rip width of 0.6 mm and pore size P of 1 mm, see table 5.1. The grid fill factor f is found by following equation Mikhailova et al. [2005]:

$$f = 1 - \frac{A_{f1}}{A_{f0}} \tag{5.1}$$

where A_{f1} and A_{f0} are the area unoccupied by the grid rod, and the total grid area respectively. The grid hydraulic diameter is calculated based on grid thickness and grid rip width and is given as:

$$d_{h,grid} = \frac{4 \cdot S \cdot D}{2 \cdot (S + D)} \tag{5.2}$$

Where S and D is the grid rod width and grid thickness respectively they are shown in figure 5.1. The corresponding Re number is calculated by following equation [Mikhailova et al., 2005]:

$$Re_{grid} = \frac{u_{grid} \cdot d_{h,grid}}{[(1-f)\,\nu]} \tag{5.3}$$

where Re_{grid} is the Re number in the grid. The velocity through the grid is calculated based on grid area unoccupied by the grid rods and the total grid area respectively. The free stream velocity is $u_{\infty} = 0.75\frac{m}{s}$ and the total area of the grid is $A_{f0} = 19.508mm^2$. The unoccupied area of the grid is $A_{f0} = 11.81mm^2$ and thus the grid velocity u_{grid} is found by following:

$$u_{grid} = \frac{u_{\infty} f_0}{f_1} \tag{5.4}$$

The same procedure is used for the calculation of grid Re number and grid velocity with the honeycomb structure.

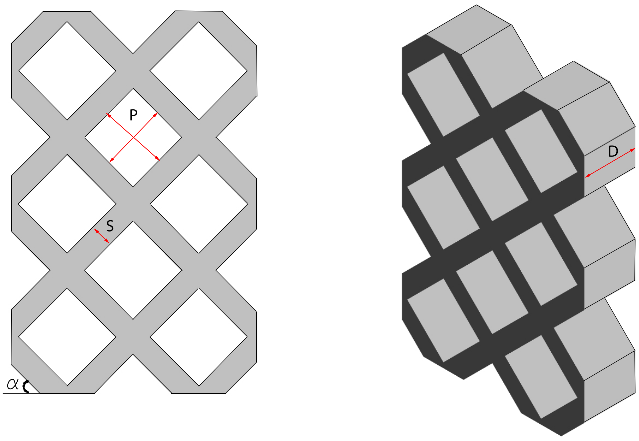

Figure 5.1. Schematic of square grid and its dimensional parameters.

Table 5.1. Dimensions of the square grid

Parameter	Dimensions	Unit
Grid pore size, P	1	[mm]
Grid thickness, D	1	[mm]
Rip width, S	0.6	[mm]
Fill factor, f	0.605	[-]
Velocity in the grid, u_{grid}	1.9	$\frac{m}{s}$
Grid Re number, Re_{grid}	231	[-]
Pore angle, α	45	[°]

The second grid is made of honeycomb structure. The honeycomb structure has been studied and tested in many years by researchers in wind tunnels test sections in order to eliminate or generate turbulences. The rip width and thickness of the honeycomb grid in this report is the same as the square grid but corresponding fill factor and grid Re number are different, see table 5.2.

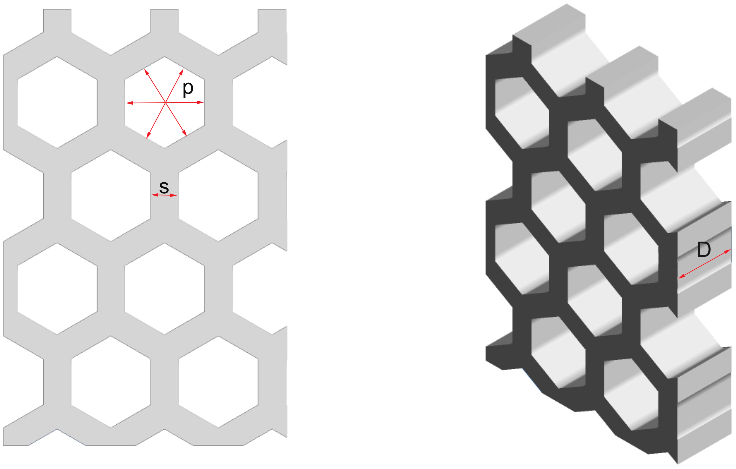

Figure 5.2. Schematic of honeycomb grid and its dimensional parameters.

Table 5.2. Dimensions of the honeycomb grid

Parameter	Dimensions	Unit
Grid pore size, P	1	[mm]
Grid thickness, D	1	[mm]
Rip width, S	0.6	[mm]
Fill factor, f	0.613	[-]
Velocity in the grid, u_{grid}	1.94	$\frac{m}{s}$
Grid Re number, Re_{grid}	241	[-]
Pore angle, α	90	[°]

Chapter

6

Computational Fluid Dynamics

This chapter presents the computational domain, meshing strategy, boundary conditions (BC's) and types of solver used in Computational Fluid Dynamic (CFD) simulation. Further it introduces the governing equations and turbulence model used therein.

An error was discovered during the post processing of the obtained CFD results. The error was discovered too late in the process to redo the simulations. The results presented in this report is obtained from simulations with constant fluid density. A quick study where this was changed for the case without grid and the case with square grid placed 10 mm from channel showed small variations in the numerical values and a slight deviation in tendencies. Meaning the difference in numerical values is not constant along the channel length. The parameter that changes the most is the average velocity where the flow accelerates along the channel yielding a gradual increase in velocity.

There are 3 general procedures in CFD: Pre-processor, solver and post-processor, see figure 6.1. The pre-processor prepares the user defined geometry, generating the mesh and setting physical properties and boundary conditions respectively. The solver integrates the governing equations of the fluid flow over each cell in the entire fluid domain. Then it discretizes the integrated equations into a system of linear algebraic equations and solving numerically the system of equations. The post-processor visualizes the produced data through contour plots, velocity vector fields, streamlines among others. The CFD simulations are done with 3 different geometries, the first is the reference geometry without

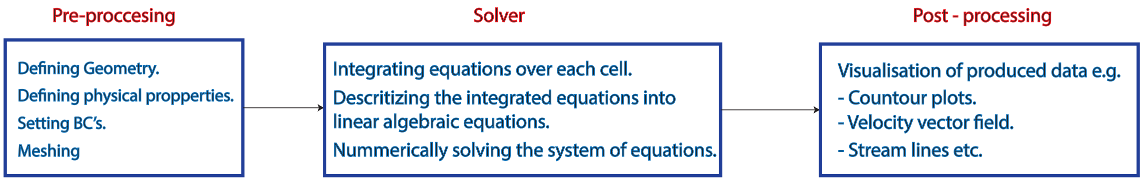

Figure 6.1. Procedure of CFD setup and modelling

grid, the second is with the square grid and the third is with the honeycomb grid. These three geometries will be referred to as cases.

6.1 Governing Equations

In this section the governing equations used in the CFD ANSYS fluent modelling will be introduced.

Before introducing the governing equations the assumptions needs to be taken into account. The assumptions in this study is made to simplify the model and reduce the time and computational resources. The assumptions made in the model are the following:

1. Steady in-compressible flow.
2. Thermophysical properties of the solids are constant.
3. Viscous heating and radiation are negligible.
4. Flow is assumed to be thermally and hydraulically fully developed.

6.1.1 Navier Stokes Equations

Navier Stokes equations are partial differential equations describing the fluid motion and are fundamental equations of fluid dynamics. Based on the assumptions above, the governing Navier Stokes equations for continuity and momentum are as following [Versteeg and Malalasekera, 2007]:

$$\frac{\partial}{\partial x_i}(\rho u_i) = 0 \tag{6.1}$$

where u, v and w are the velocity components in direction of x, y and z, respectively.

For the momentum equation it is [ANSYS, 2018c]:

$$\underbrace{\frac{\partial u_j u_i}{\partial x_j}}_{\substack{Convective\\ acceleration}} \underbrace{= -\frac{1}{\rho}\frac{\partial p}{\partial x_i}}_{\substack{Pressure\\ forces}} + \underbrace{\frac{\partial}{\partial x_j}\left(\mu \frac{\partial u_i}{\partial x_j}\right)}_{Viscous \quad forces} + \underbrace{\rho g}_{\substack{Gravity\\ forces}} \tag{6.2}$$

6.1.2 Reynolds Average Navier Stokes Equation

In the Reynolds Average Navier Stokes equations (RANS) the instantaneous variables in Navier-Stokes equations are decomposed into a mean (time average) and fluctuation components (i=1,2,3). For the velocity component the equation becomes Versteeg and Malalasekera [2007]:

$$u_i = \bar{u}_i + u_i^{'} \tag{6.3}$$

where $\bar{u}$ and $u^{'}$ are the mean and fluctuation velocity respectively. Likewise for pressure and other quantities it is:

$$\varphi_i = \bar{\varphi}_i + \varphi_i^{'} \tag{6.4}$$

where φ denotes a scalar such as pressure, energy or species concentration. Substituting the expressions into the instantaneous continuity and momentum equations and taking the time average (dropping the overbar on the mean velocity $\bar{u}$) yields the following RANS equations for continuity and momentum [ANSYS, 2018c]:

$$\frac{\partial}{\partial x_i}(\rho u_i) = 0 \tag{6.5}$$

$$\underbrace{\frac{\partial u_j u_i}{\partial x_j}}_{\substack{Convective\\ acceleration}} = \underbrace{-\frac{1}{\rho}\frac{\partial p}{\partial x_i}}_{\substack{Pressure\\ forces}} + \underbrace{\frac{\partial}{\partial x_j}\left(\mu \frac{\partial u_i}{\partial x_j}\right)}_{Viscous \quad forces} + \underbrace{\rho g}_{\substack{Gravity\\ forces}} + \frac{\partial}{\partial x_j}\underbrace{\left(-\rho \bar{u}_i^{'} u_j^{'}\right)}_{\substack{Reynolds\\ stresses}} \tag{6.6}$$

The additional term $-\rho u_i^{'} u_j^{'}$ that appears in 6.6 are known a the Reynolds stresses. These Reynolds stresses must be modelled in order to close equation 6.6 and thereby a turbulence model needs be introduced and applied.

6.1.3 Turbulence Models

There exist many turbulence models for different engineering applications regarding fluid mechanics, aerodynamics etc. No turbulence models are universally accepted as being superior for all class of problems. In order to make appropriate an choice of a turbulence model for this study some of the turbulence models are examined in terms of their capabilities and limitations. These turbulence models are the following:

- **Large eddy simulations (LES):** The model is based on the approach of solving large turbulent structures in space and time down to the smallest grid limit everywhere in the flow. LES requires very fine mesh in the near wall region in order to resolve turbulence scale structures. This model requires excessively high resolution for wall bounded layer and is computationally costly and time consuming [ANSYS, 2018b].
- **Spalart-Allmaras One-Equation Model:** Solves a modelled transport equation for the kinematic eddy viscosity. The model was primary designed for aeronautics and aerospace applications involving wall bounded flows. Has shown good results for boundary layers subjected to adverse pressure gradients but is not recommended to use the model as general purpose model, as it is not well calibrated for free shear flows [ANSYS, 2018b].
- **k-ϵ Model:** Two equation model which is widely used in industrial CFD. Solves two transport equations and model the Reynolds Stresses using the Eddy Viscosity approach. It is robust, economical and has a reasonable accuracy for a wide range of turbulent flows. The drawback of k-ϵ model is its insensitivity to adverse pressure gradients and boundary layer separation. The model typically predict a delayed and reduced separation relative to observations which results in overly optimistic design evaluations for flows separating from smooth surface [ANSYS, 2018b].
- **Standard k-ω model:** The standard k-ω model can be integrated without additional terms through the viscous sub-layer. This model is typically better at predicting adverse pressure gradients boundary layers flows and separation. The

drawback of this model is that it is highly sensitivity of the solution depending on the free stream values of k and ω outside the shear layer. The use of the standard k-ω is not generality recommended in ANSYS Fluent [ANSYS, 2018b].

- **SST-k-ω:** The SST-k-ω model has been designed to avoid the free stream sensitivity of the k-ω model. The mode is a hybrid model that transforms k-ϵ model into k-ω in the near wall-region and uses the standard k-ϵ in the free stream region. The model is highly used model for aerodynamic flows and it is more accurate in predicting the details of the wall boundary layer characteristics than the Spalart-Allmaras model [ANSYS, 2018b].

By the research of different turbulence models, the most suitable one for this study, which requires an accurate prediction and detailed characteristics of boundary layer, SST-$k-\omega$ has been chosen to be utilized in the commercial ANSYS CFD modelling software.

6.1.4 SST-k-ω

SST $k-\omega$ computes the Reynolds stresses as two-equation models by the use of Boussinesq hypothesis. Boussinesq was the first to close the Reynolds stresses problem by providing an expression for the Reynolds stresses and introducing eddy viscosity. Boussinesq approach relates Reynolds stresses to the mean velocity gradient. The expression is given as following: [Versteeg and Malalasekera, 2007]:

$$\tau_{ij} = -\rho\overline{u_i'u_j'} = -\frac{2}{3}\rho k\delta_{ij} = \mu_t\left(\frac{\partial U_i}{\partial x_j} + \frac{\partial U_j}{\partial x_i}\right) - \frac{2}{3}\rho k\delta_{ij} \tag{6.7}$$

here $\mu_T = \frac{\rho k}{\omega}$ is eddy viscosity, k is the turbulent kinetic energy $k = \frac{1}{2}\cdot(\overline{u'^2} + \overline{v'^2} + \overline{w'^2})$, ω is the specific turbulent dissipation rate and δ is Kronechker delta.

6.1.5 Energy Equations

The energy equation is a mathematical statement which based on the physical law and derived from the first law of thermodynamics which states [Versteeg and Malalasekera, 2007]:

$$\begin{bmatrix} Rate\ \ of\ \ increase \\ of\ \ energy\ \ of \\ fluid\ \ particle \end{bmatrix} = \begin{bmatrix} Net\ \ rate\ \ of \\ heat\ \ added\ \ to \\ fluid\ \ particle \end{bmatrix} + \begin{bmatrix} Net\ \ rate\ \ of\ \ work \\ of\ \ energy\ \ of \\ fluid\ \ particle \end{bmatrix} \tag{6.8}$$

The energy equation for the fluid is given as [Versteeg and Malalasekera, 2007]:

$$u_j\frac{\partial T_f}{\partial x_j} = \frac{1}{\rho c_{pf}}\frac{\partial}{\partial x_j}\left(k_f\frac{\partial T_f}{\partial x_j}\right) \tag{6.9}$$

where c_{pf} is the fluid heat capacity, T_f is the temperature of the fluid and k_f is the thermal conductivity of the fluid.

The energy equation for the solid region [Versteeg and Malalasekera, 2007]:

$$\frac{\partial}{\partial x_j}\left(k_s\frac{\partial T_s}{\partial x_j}\right) = 0 \tag{6.10}$$

where k_s is the thermal conductivity of the solid and T_s is the temperature of the solid.

6.2 Near Wall Treatment

Near wall region is categorized into 3 different regions: Viscous sub-layer region, buffer layer region and log-law region. The viscous sub-layer region, is a region where the fluid adjacent to the wall is dominated by the viscous effects. The region is extremely thin ($y^+ < 5$) and thus the shear stress and wall shear stress τ_w is equal and constant throughout the layer. In that region the mean velocity and wall distance y has linear relationship [Versteeg and Malalasekera, 2007].

The buffer layer region consist of the viscous sub-layer and the log-law layer. Here the value y^+ is between 5 and 30. In that region the viscous and turbulent stresses are of the same magnitude [Versteeg and Malalasekera, 2007].

Log-law layer region, is the region where the viscous and turbulent effects are important. The y^+ values lies in a range of ($30 < y^+ < 500$), where the shear stress τ varies with the distance from the wall [Versteeg and Malalasekera, 2007].

The flow behaviour of turbulences in the near wall regions differs from that of a free stream flow. In these regions, the flow velocity depends mainly on the wall distance y away from the wall, fluid density ρ, fluid viscosity μ and wall shear stress τ_w. mathematically,these can be formulated as following [Versteeg and Malalasekera, 2007]:

$$u^+ = \frac{u}{u_\tau} = f(\frac{\rho u_\tau y}{\mu}) = f(y^+) \tag{6.11}$$

where u^+ and y^+ are dimensionless numbers, $u_\tau = \sqrt{\frac{\tau_w}{\rho}}$ is friction velocity. Eq. 6.11 is also called law of the wall.

6.2.1 Estimation of First Cell Height

The first cell height is the distance of the first interior node from the wall. In this study it is utilized in order to capture the boundary layer behaviour. As mentioned, the viscous sub-layer is between the $0 < y^+ < 5$ and the dimensionless y^+ value in this study is set to 5. The wall distance y is calculated by following procedure Yin [2016]:

$$Re = \frac{\rho \cdot u \cdot d_c}{\mu} \tag{6.12}$$

$$f = \frac{1}{(0.79 \cdot \ln{(Re)} - 1.64)^2}[-] \tag{6.13}$$

$$\tau_{wall} = \frac{1}{2} \cdot \frac{f}{4} \cdot \rho \cdot u^2 \tag{6.14}$$

$$u_\tau = \sqrt{\frac{\tau_{wall}}{\rho}} \tag{6.15}$$

$$y = \frac{y^+ \cdot \mu}{\rho \cdot u_\tau} \tag{6.16}$$

where f is friction coefficient. The estimated first cell height is given in table 6.1 for the channel and the grids.

Table 6.1. First cell height of channel and grids

	Square grid	Honeycomb grid	Channel	
Reynolds number, Re	231	241	265	[-]
First cell height, y	0.0617	0.0617	0.217	[mm]

These values are used in all CFD simulations in order to predict and capture the turbulences in the near wall regions.

6.3 Dimensional Description

The computational domain considered in this study is limited to a single channel, as shown in figure 2.5.

The cross sectional dimensions of the single channel are depicted in figure 6.2 The dimensions are listed in table 6.2.

The dimensions of the computational domains fluid direction are listed in table 6.3 and on the corresponding figure 6.3. The distance between the grid and the inlet of the channel is varied in 5 different distances, 20 mm 10 mm, 5 mm, 3 mm and 2.5 mm. All dimensions are the same in the two cases with the two different types of grid. The case without the grid has the same dimensions except that the part of fluid domain between grid and channel is removed from that geometry.

Table 6.2. Dimensions of the channel corresponding to figure 6.2.

Location of figure	Dimensions	Unit
A	3.56	[mm]
B	5.48	[mm]
C	1.06	[mm]
D	2.5	[mm]
E	2.3	[mm]
F	0.2	[mm]

Table 6.3. Dimensions of the channel corresponding to figure 6.3.

Location of figure	Dimensions	Unit
A	40	[mm]
B	1	[mm]
C	20, 10, 5, 3, 2.5	[mm]
D	70	[mm]
E	30	[mm]

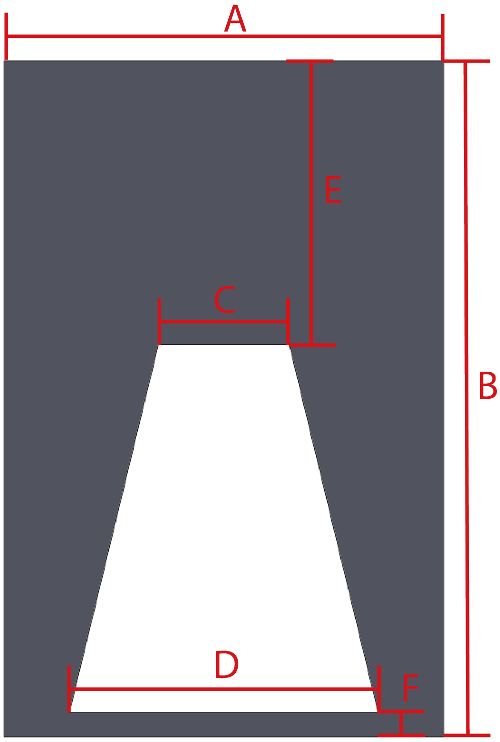

Figure 6.2. Cross sectional view of a single channel.

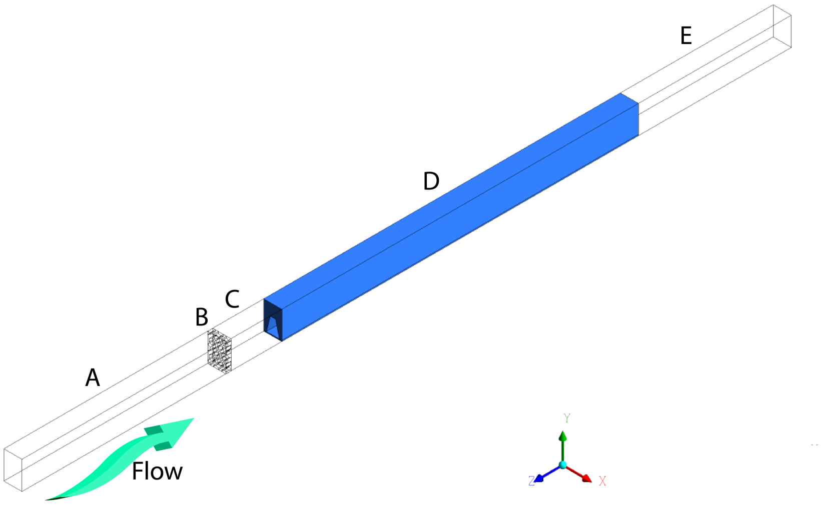

Figure 6.3. The whole computational domain with dimensional description in the flow direction.

6.4 Meshing Quality

This section explains the quality of the generated mesh. The quality description only applies for the case with the honeycomb-grid. But the other meshes are similar in quality. The meshes are primarily hexahedral elements. Sections of the mesh are shown in figure 6.4 where it is shown that the mesh between grid and channel is refined and 6.5 where it shows the fine mesh inside the grid where inflation are used in the fluid domain.

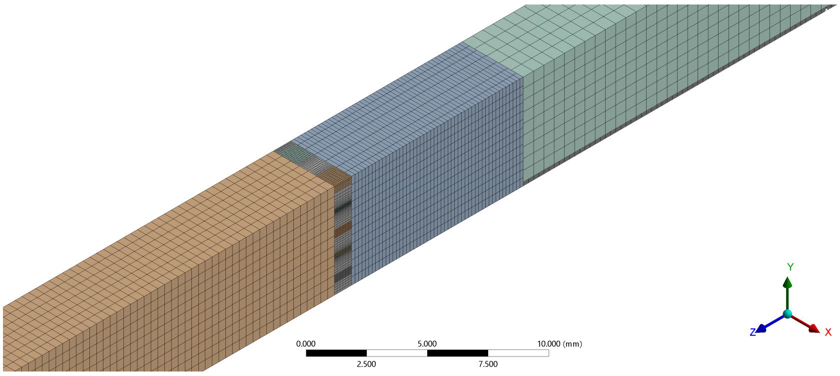

Figure 6.4. The mesh in the region between grid and channel.

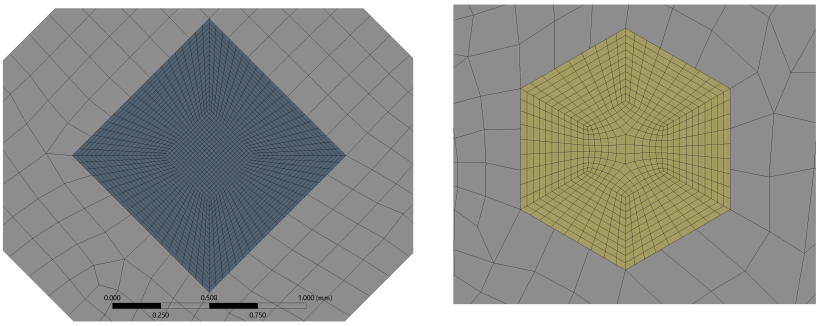

Figure 6.5. The mesh in the middle of each grid.

6.4.1 Orthogonal Quality

The orthogonal quality describes the cells placement compared to the adjacent cells.

The calculation of orthogonal quality is done by the following [ANSYS, 2010]:

$$max\left[\frac{\overrightarrow{A_i}\cdot\overrightarrow{f_i}}{\left|\overrightarrow{A_i}\right|\left|\overrightarrow{f_i}\right|}\quad,\quad\frac{\overrightarrow{A_i}\cdot\overrightarrow{c_i}}{\left|\overrightarrow{A_i}\right|\left|\overrightarrow{c_i}\right|}\right] \tag{6.17}$$

Where $\overrightarrow{A_i}$ is the face normal vector, $\overrightarrow{f_i}$ is the vector from cell centroid to face center and $\overrightarrow{c_i}$ is a vector from cell centroid to the cell centroid of the adjacent cell that shares the face as shown in figure 6.6.

From the definition of orthogonal quality it is seen that a value of 1 means that the vectors of the cells are parallel. The highest quality is 1 and lowest is 0. The percentage distribution of orthogonal quality in the generated mesh is tabulated in table 6.4 and the maximum, minimum and average values are shown in table 6.5.

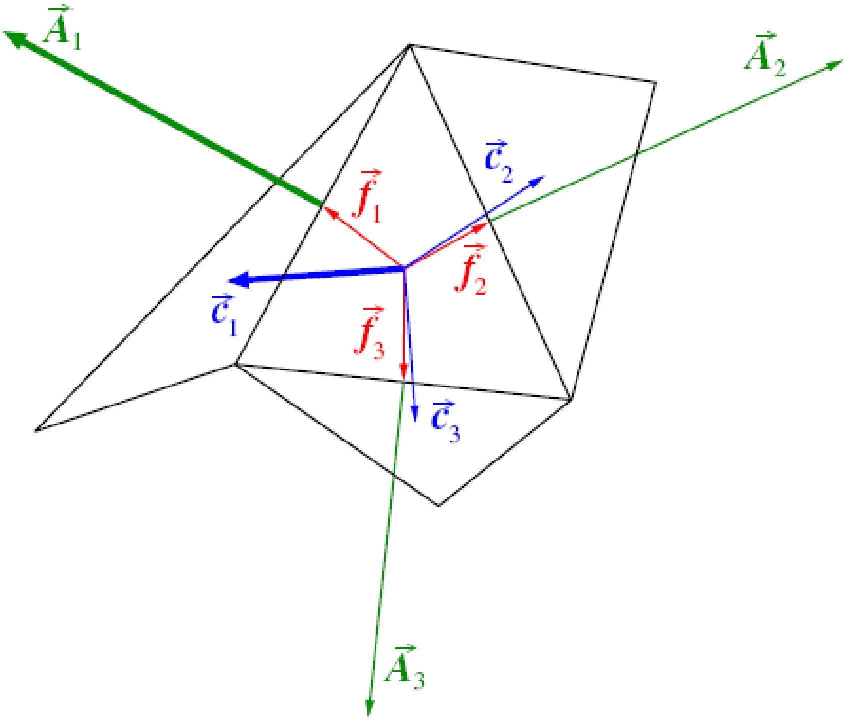

Figure 6.6. Vectors to calculate orthogonal quality [ANSYS, 2010].

Table 6.4. Distribution of orthogonal quality in percentage of total cell number.

Value	Percentage
0.5 - 0.6	0.349
0.6 - 0.7	2.14
0.7 - 0.8	2.5
0.8 - 0.9	5.4
0.9 - 1.0	89.1

Table 6.5. Orthogonal quality max, min and avg values.

Maximum	Minimum	Average
1.0	9.4207e-002	0.94206

From the criteria of orthogonal quality the used mesh is considered as high orthogonal quality with an average value of 0.94206.

6.4.2 Aspect Ratio

The aspect ratio of a cell is defined as the ratio between the longest and shortest side as shown in figure 6.7. The aspect ratio is mathematically defined as: $AR = B/A$

The aspect ratio on the generated mesh is distributed as tabulated in table 6.6. The maximum, minimum and average aspect ratio is given in table 6.7.

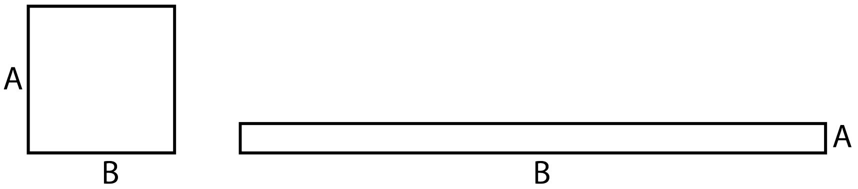

Figure 6.7. Definition of aspect ratio, the square on the left has the optimal aspect ratio of 1 and the one on the right has an aspect ratio of 20.

An aspect ratio of 1 is the optimal and it is shown from the table that the generated mesh has a majority of cells with very low aspect ratio.

Table 6.6. Distribution of aspect ratio.

Value	Percentage
1 - 3	84.2
3 - 6	6.97
6 - 9	4.45
9 - 12	3

Table 6.7. Aspect ratio max, min and avg values.

Maximum	Minimum	Average
26.645	1.0123	4.1358

6.4.3 Cell Skewness

The skewness is a measure of how much the cell angles deviates from a perfect cell shape as shown in figure 6.8.

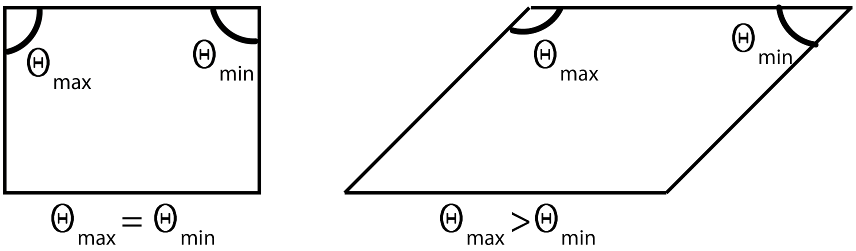

Figure 6.8. Definition of skewness, the square on the left is perfectly equiangular, and the one on the right is skewed.

It is calculated as [ANSYS, 2018a]:

$$max[\frac{\Theta_{max}-\Theta_e}{180-\Theta_e},\frac{\Theta_e-\Theta_{min}}{\Theta_e}] \tag{6.18}$$

where Θ_{max} is the maximum angle in the cell, Θ_{min} is the minimum angle in the cell and Θ_e is the equiangular angle for a cell, $\Theta_e = 90$ for hexahedral cells. From the definition it is clear that 0 equals and equiangular cell and thereby the best obtainable skewness. Further it is seen that a skewness of 1 is the worst.

The distribution of cell percentage of 83.2 % with a given skewness is given in table 6.8 where it is seen that a high percentage of the cells is below 0.2 in skewness. Table 6.9 shows the maximum, minimum and average skewness. Here it is shown that the average is 0.16901 which is classified as excellent in the meshing user's guide. According to ANSYS [2018a] a skewness of up to 0.5 is still considered as good.

Table 6.8. Distribution of skewness.

Value	Percentage
0 - 0.1	43.4
0.1 - 0.2	39.8
0.2 - 0.3	5.69
0.3 - 0.4	2.9
0.4 - 0.5	3.84
0.5 - 0.6	2.8

Table 6.9. Skewness max, min and avg values.

Maximum	Minimum	Average
0.97201	2.6571e-010	0.1677

6.5 Grid Independence Study

Grid independence study has been conducted in this study in order to validate the reliability of the CFD simulations. The grid independence study insures that the obtained results are independent of the grid size. The procedure of grid independence study has been such that the base grid has been refined and coarsened by doubling and halving the number of elements respectively. The evaluation parameter was the pressure distribution throughout the channel in all different grid sizes. The pressure loss for all three grid sizes is illustrated in figure 6.9.

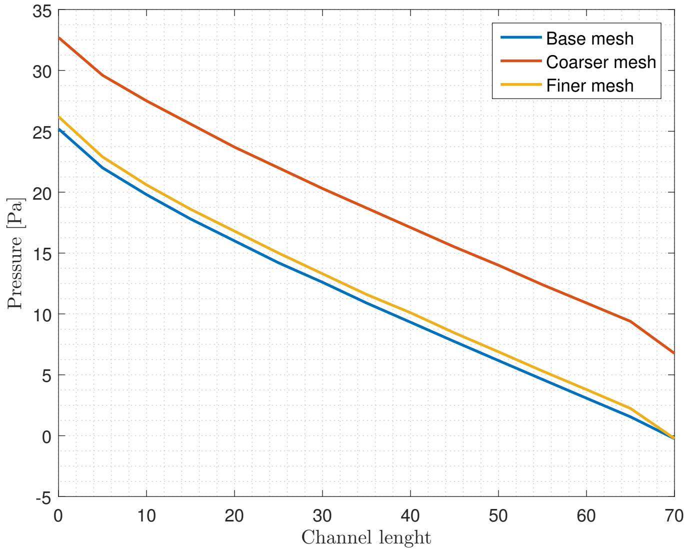

Figure 6.9. Evaluations of pressure loss throughout the channel by three different grid sizes

It is clearly seen from figure 6.9 that the pressure loss deviation is much higher with the coarser mesh than the fine. This indicates that the number of elements will be highly dependent on the mesh if the number of elements were halved. Table 6.10 shows the mean percentage deviation of the pressure distribution throughout the channel. The mean percentage deviation of pressure distribution throughout the channel of the coarser grid is 67.4 % from the base grid. For the finer grid, the mean percentage deviation is 6.27 %. A mean percentage deviation of 6.27 % is concluded to be in an acceptable range due to the fact that the maximum amount of elements available in ANSYS CFD is 512 000 cells (Student licence).

Table 6.10. Mean % deviation of the pressure distribution of different grid size from base grid

	Base grid	Coarser mesh	Finer mesh	
Number of elements	485520	267830	856429	[-]
Average pressure distribution	11.3872	19.0637	12.1015	[Pa]
%-deviation	0	67.4	6.27	%

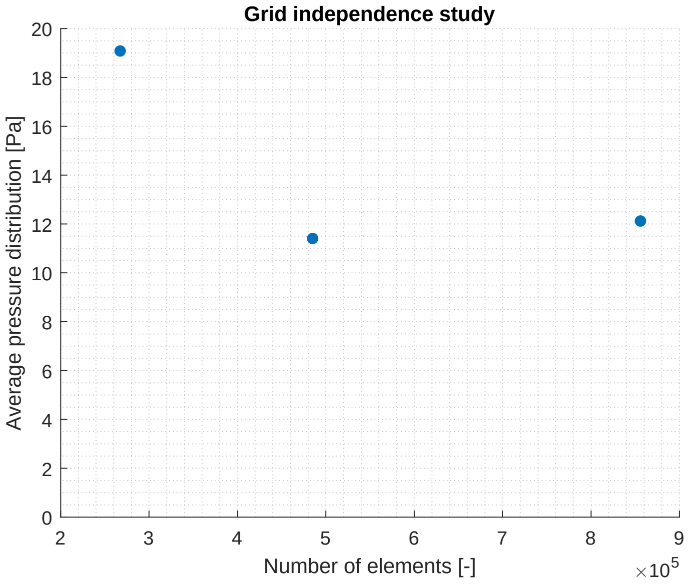

Figure 6.10. Average pressure distribution in the channel with base grid, coarser grid and finer grid

Figure 6.9 shows the average pressure distribution vs. number of element. It is clearly seen that the solution is dependent on the grid when the mesh is coarsened. Observing the finer grid and the base grid it can be concluded that the solution is independent of the grid and within an error of 6 % which is considered acceptable.

6.6 Boundary Conditions (BC's) and Material Properties

In this section boundary conditions (BC's) and material properties will be presented.

The computational domain consist of one single channel with corresponding cross-sectional grid in order to simplify the model and save computational time and resources. Thus to accommodate for realistic results, on each side of the computational domain a symmetry is applied as shown in figure 6.11.

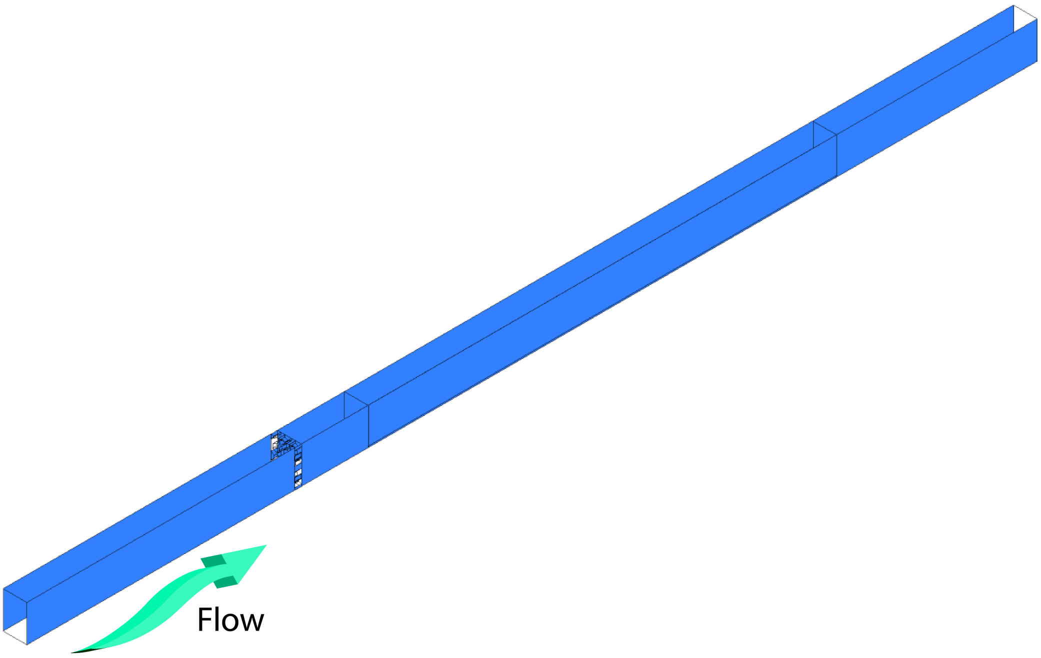

Figure 6.11. The whole computational domain with applied symmetry shown on the blue faces.

For the inlet (velocity inlet) the BC is following:

$$u = u_{in}, \quad v = 0, \quad w = 0 \quad and \quad T = T_{in} \tag{6.19}$$

For the Outlet (pressure outlet):

$$p = p_{out} \tag{6.20}$$

At the interfaces between fluid-solid regions:

$$u = 0, \quad v = 0, \quad w = 0 \quad and \quad T = T_{in} \tag{6.21}$$

Constant heat flux applied at the bottom of the channel wall:

$$q_w = -k_s \frac{\partial T_s}{\partial n} \tag{6.22}$$

For other solid walls and symmetric boundaries:

$$-k_s \frac{\partial T_s}{\partial n} = 0 \tag{6.23}$$

Material properties are all listed in table 6.11 [Farah et al., 2016], [Shahsavari et al., 2012] [AZoM, 2002].

Table 6.11. Material properties

	Air at 25 °C	GDL	Graphite	PLA	
Density, ρ	1.225	2000	1625	1250	[kg/m^3]
Specific heat capacity , c_p	1006.43	840	770	1590	[J/kg K]
Thermal conductivity, k	0.0242	0.7	60	0.11	[W/m^2 K]
Viscosity, μ	1.7894e-05	-	-	-	[kg/m s]

6.7 Solver Type and Solution Method

In this section solver type and solution method used in the modelling will be presented.

In the modelling pressure-based solver is utilized and the velocity formulation is set to absolute. The time is steady state and gravity is applied in the y-coordinate direction. The SST-k-ω model is used and convergence criteria is set to default, 10^{-6} for continuity and 10^{-3} for velocities in each direction, energy, k and ω.

In CFD commercial package (ANSYS FLUENT) parameters associated with the solutions needs to be utilized in the calculations and thereby a solution method must be applied. The Navier Stokes equations are solved using finite volume method (FVM). The standard scheme is utilized for pressure discretization and SIMPLE algorithm is used to solve pressure-velocity coupling. momentum and energy equations are solved using second-order-upwind-scheme.

6.8 Results From CFD Simulations

This section presents and discusses the results of the CFD simulations. The simulations has been conducted with two different inlet velocities 0.75 m/s and 1 m/s. As described in section 6.3 the distance between the grid and the channel inlet is variable and the simulated in five different positions. All data presented here is, unless otherwise specified, exported in xy-planes distributed along the channel length z-direction with 5 mm between each plane, the planes and placement of these are shown in figure 6.12.

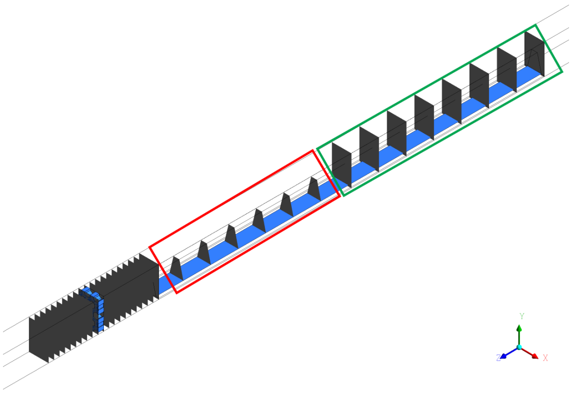

Figure 6.12. The different types of planes and distribution of planes used.

6.8.1 Temperatures

The temperatures is exported as area weighted average values in the whole computational domain, that is covering both solid and fluid part of the cross section as shown in the green box of figure 6.12. It it chosen to focus on the average of the temperature for both fluid and solid part, since the temperatures for the fluid domain only, the temperature difference between the three cases, no grid, square grid and honeycomb grid is around 0.1 K. The small deviation in fluid domain temperature is shown in figure 6.13.

Temperatures at 0.75 m/s

The corresponding full domain temperature is shown in figure 6.14 here it is shown that the average temperature decreases when implementing the two different types of grid. The figure shows that the square grid results in the lowest temperature. The outlet temperature without grid is 341.06 K and with the grid placed 10 mm before the channel the outlet temperatures are 340.35 K and 340.94 K for square grid and honeycomb grid respectively.

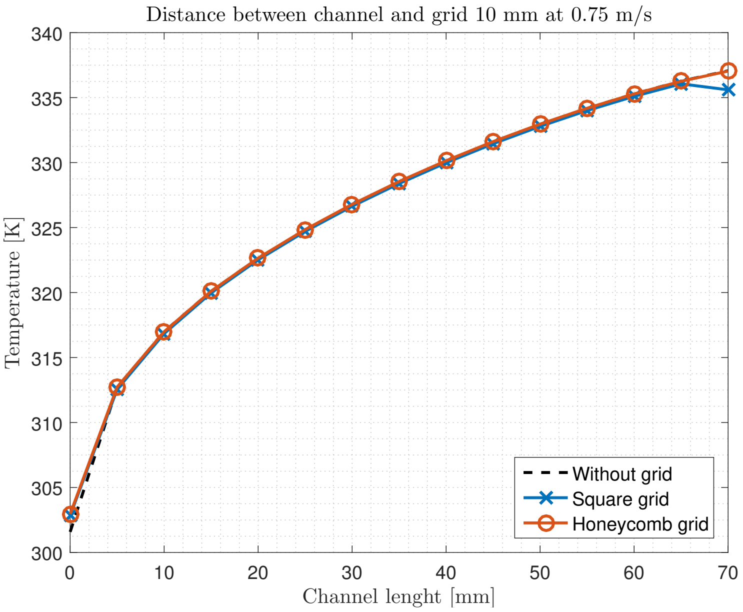

Figure 6.13. Example of the small variation of fluid domain temperatures with the grid placed at 10 mm before the channel and inlet velocity of 0.75 m/s.

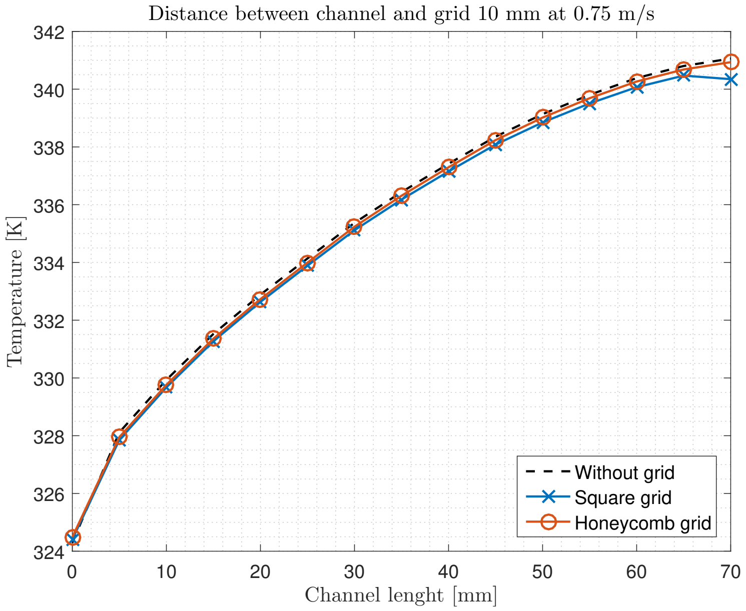

Figure 6.14. Temperature variation with grid placed 10 mm before the channel with an inlet velocity of 0.75 m/s.

Figure 6.15 and 6.16 shows the temperatures for varying distances of the two types of grid. As can be seen from the figures the grids closer to the channel results in a lower temperature. It is evident that the temperature decrease is higher on the figure with the square grid.

Figure 6.17 shows the maximum computational domain temperature in the different cases. From these results it is obvious that the square grid provides the largest decrease in temperature. Further it shows that the temperature decrease is biggest in the cases where the grid is placed closer to the channel entry. The largest difference is seen with the square grid placed 2.5 mm from the channel inlet and here the difference is 0.634 K. Looking at the values for the simulation where the distance is 20 mm it can be seen that the temperature in the case with honeycomb grid is almost identical to the case without grid. This indicates that the effect of the honeycomb grid is heavily reduced at this distance.

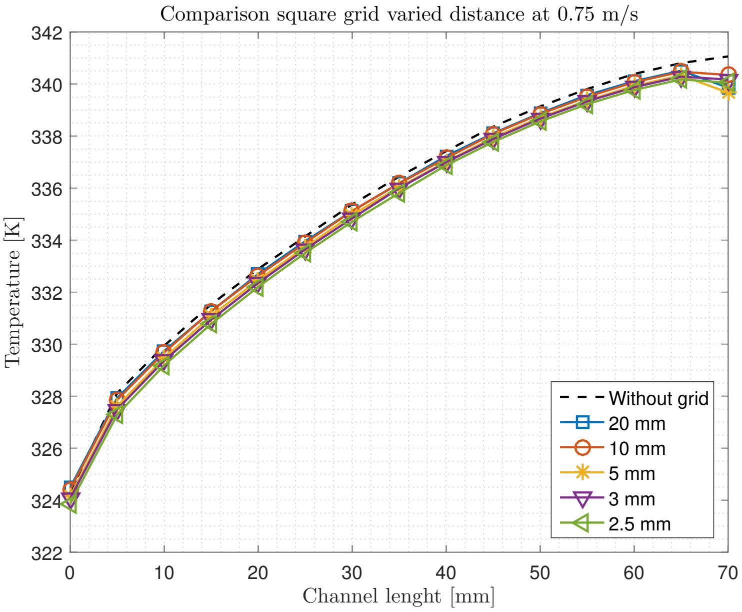

Figure 6.15. Temperature variation with square grid placed at different distances before the channel with an inlet velocity of 0.75 m/s.

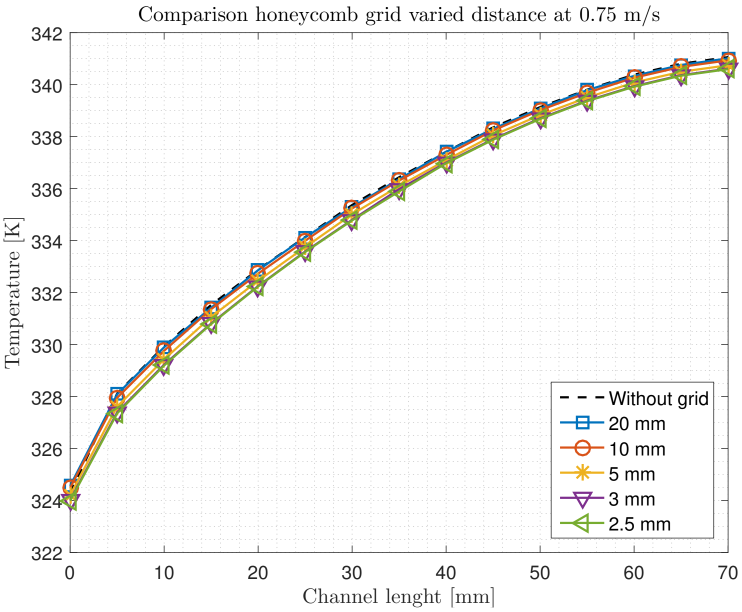

Figure 6.16. Temperature variation with honeycomb grid placed at different distances before the channel with an inlet velocity of 0.75 m/s.

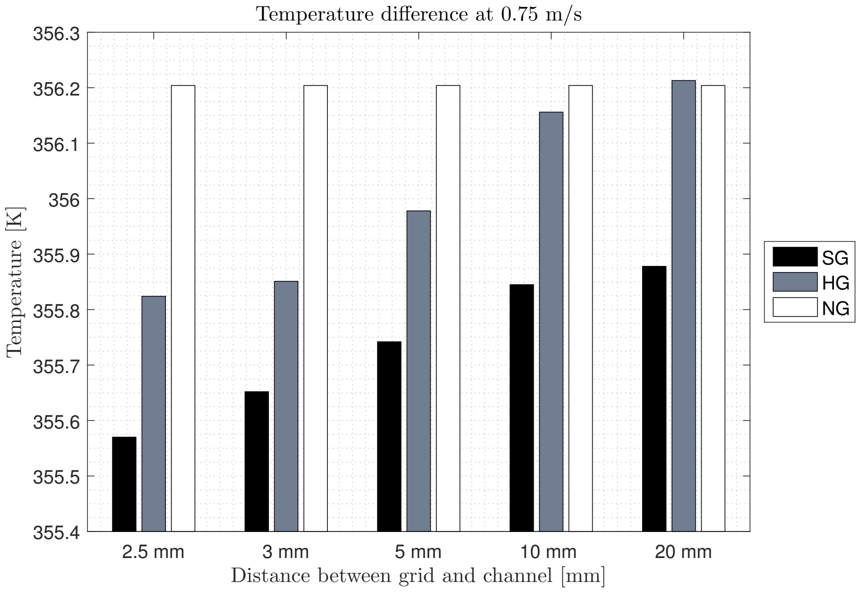

Figure 6.17. Variation in maximum temperature with an inlet velocity of 0.75 m/s.

Temperatures at 1.0 m/s

Figure 6.18 shows a clear decrease in temperature by implementing the grid. At inlet velocity of 1 m/s the effect of the grid is even more noticeable than on figure 6.14. In this case an outlet temperature of 333.09 K is reached for the case with no grid. Where the two cases with grids reach temperatures of 331.83 K and 332.57 K with square grid and honeycomb grid respectively.

In figure 6.19 and 6.20 the same effect as with the inlet velocity of 0.75 m/s with lowest temperatures in the cases where the grid is closest to the channel. Looking at figure 6.19 alone the curve for 3 mm shows deviation from the tendencies of the other curves, since the graph for 3 mm has a higher temperature than the 5 mm and 10 mm plots.

Figure 6.21 shows the maximum temperature in the whole computational domain for an inlet velocity of 1 m/s the trend is the same as for the previous case with inlet velocity of 0.75 mm. This results shows that the effect of the grid appears to be higher with higher velocities. The maximum difference in this simulation is also the square grid placed 2.5 mm from the channel inlet, where the temperature difference is 1.001 K. Figure 6.21 shows the same odd behavior for the 3 mm square grid results as shown in figure 6.19, where the temperature is higher than for the distances of 5 mm and 10 mm.

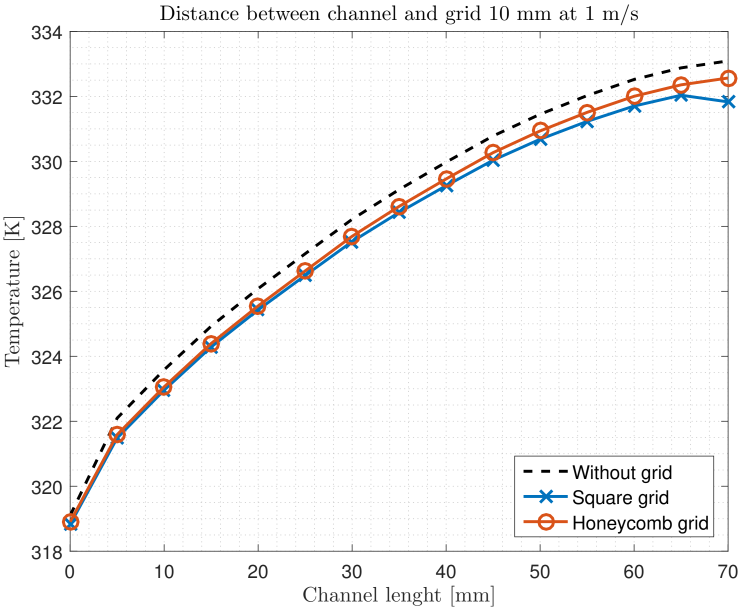

Figure 6.18. Temperature variation with grid placed 10 mm before the channel with an inlet velocity of 1 m/s.

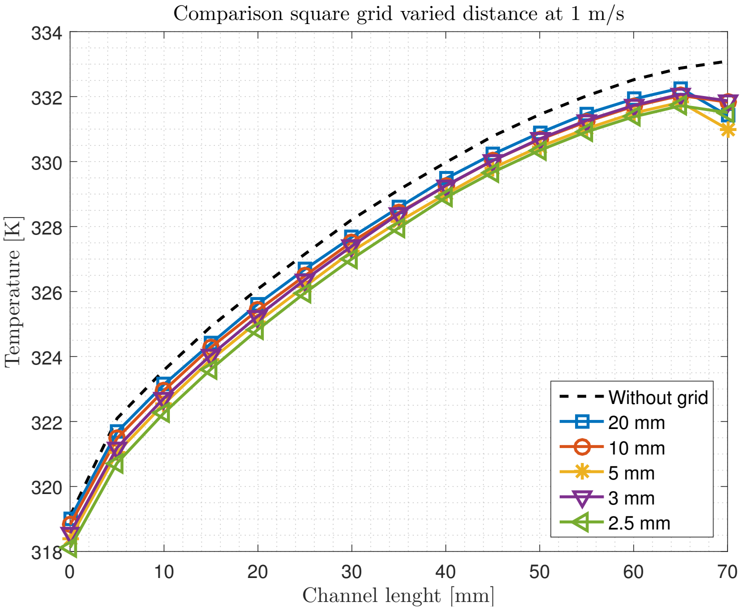

Figure 6.19. Temperature variation with square grid placed at different distances before the channel with an inlet velocity of 1 m/s.

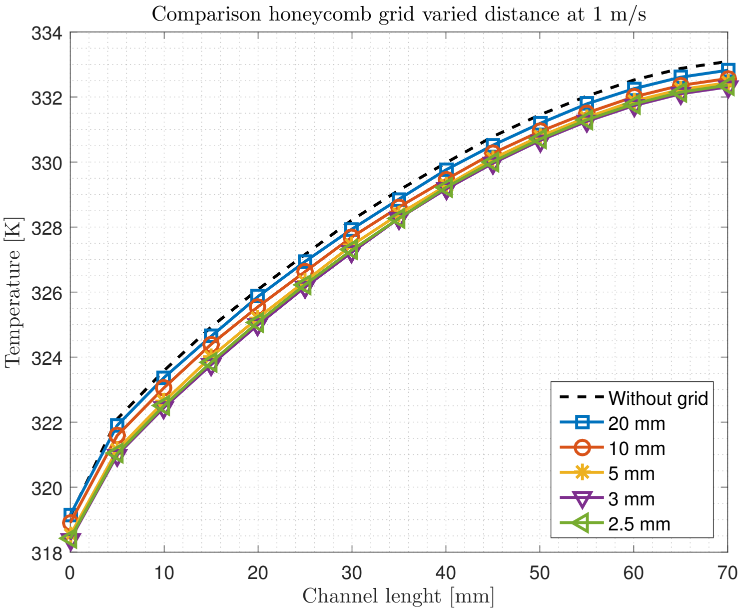

Figure 6.20. Temperature variation with honeycomb grid placed at different distances before the channel with an inlet velocity of 1 m/s.

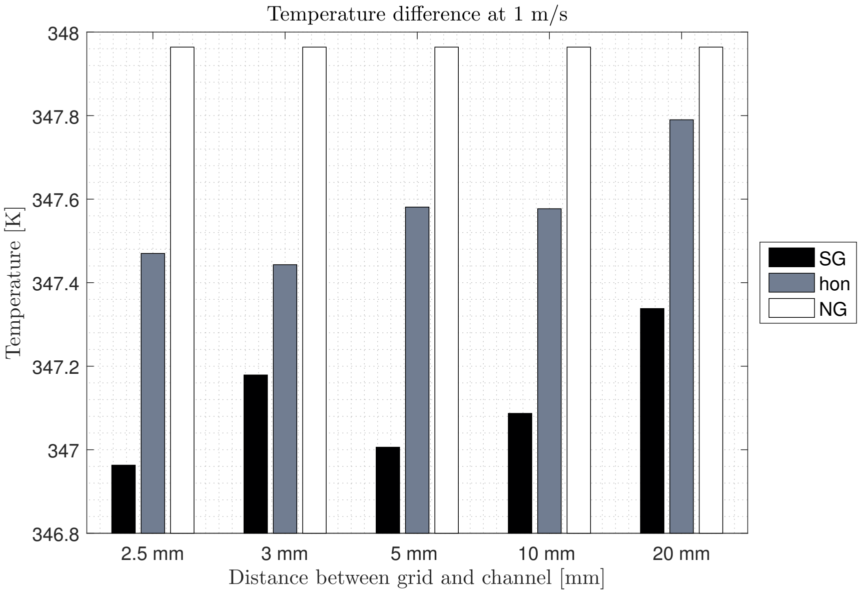

Figure 6.21. Variation in maximum temperature with an inlet velocity of 1 m/s.

6.8.2 Velocities

This section shows the velocities obtained in the channel. The velocities is area average values in planes covering the fluid domain. The planes are shown in the red box of figure 6.12.

Velocities at Inlet Velocity of 0.75 m/s

The grid increases the velocity in the inlet of the channel as shown in figure 6.22, where a slight increase from 2.86 m/s in the no grid case to 2.93 m/s in the two cases with grid.

A comparison of velocities at different distances of both types of grid is shown in figure 6.23 and 6.24 where it is evident that the closer the grid is to the channel inlet the higher is the velocity in the beginning of the channel. Further it is seen that the channel inlet velocities in the case with honeycomb grid is slightly higher than in the case with square grid.

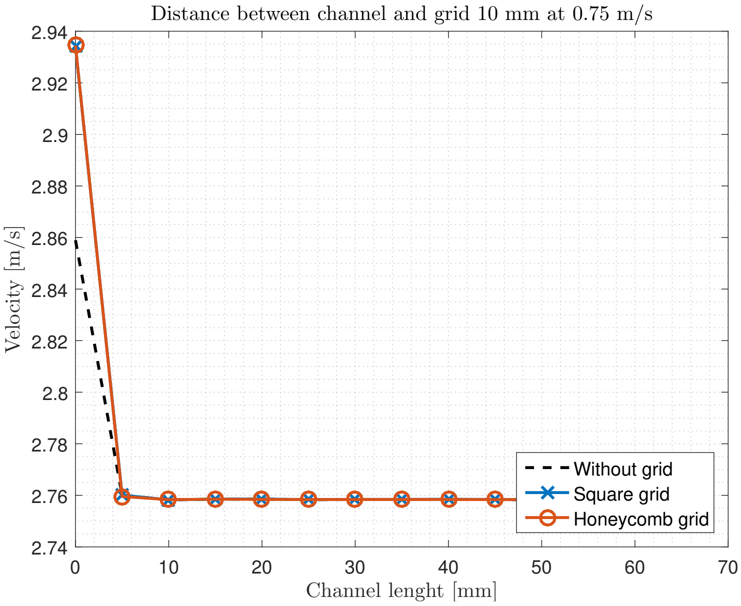

Figure 6.22. Velocity variation with grid placed 10 mm before the channel with an inlet velocity at 0.75 m/s.

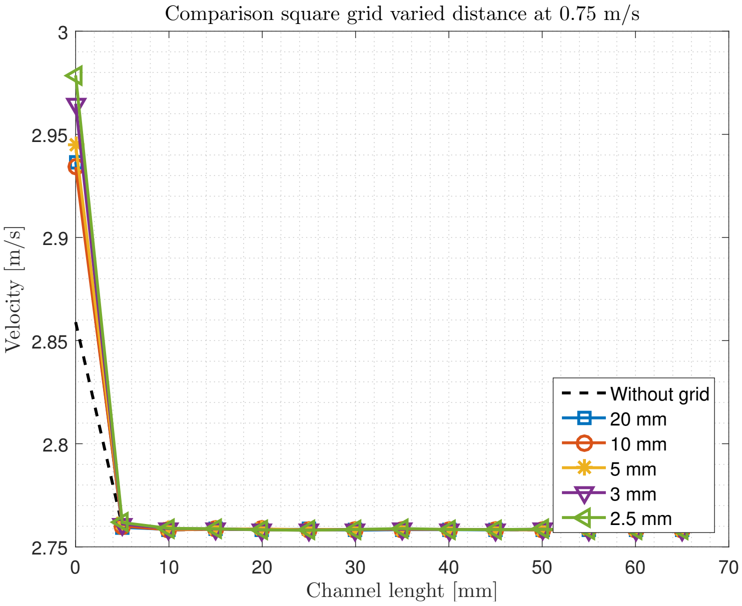

Figure 6.23. Velocity variation with square grid placed at different distances before the channel with an inlet velocity at 0.75 m/s.

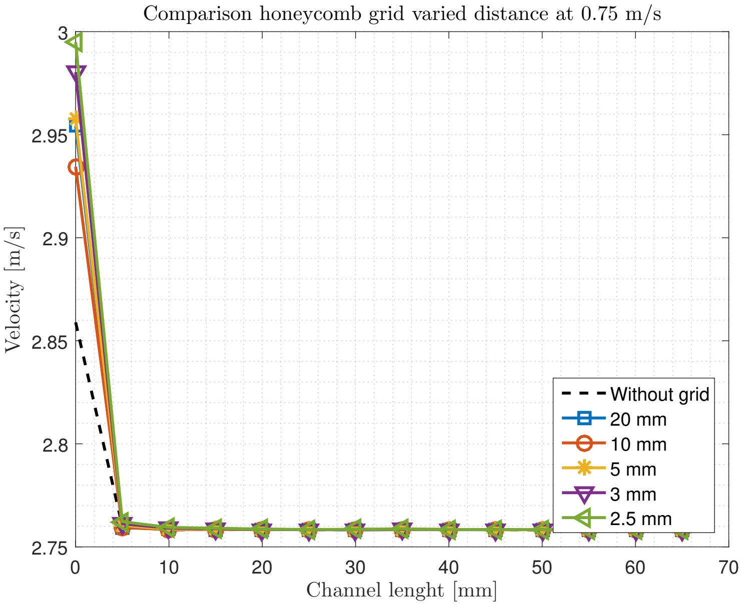

Figure 6.24. Velocity variation with honeycomb grid placed at different distances before the channel with an inlet velocity at 0.75 m/s.

Velocities at Inlet Velocity of 1 m/s

The results for the simulation conducted at inlet velocity of 1 m/s shows the same tendencies as the results for inlet velocity of 0.75 m/s. The results at 1 m/s have velocities as would be expected.

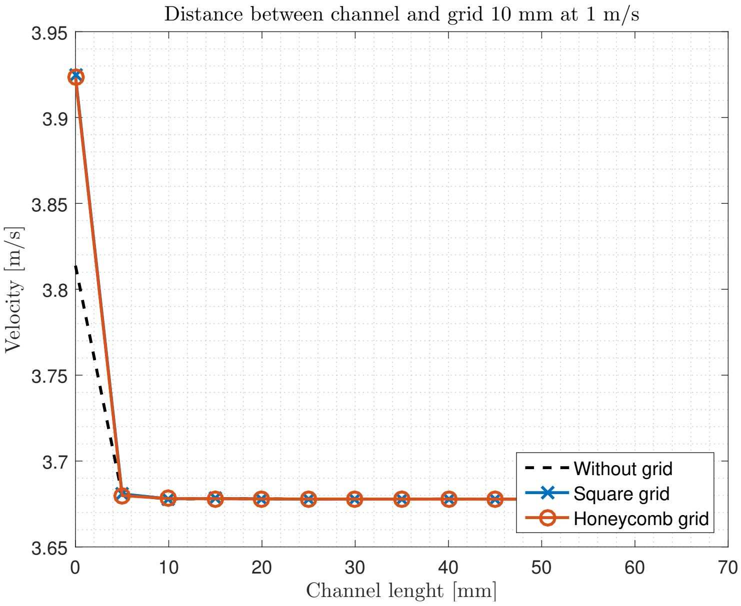

Figure 6.25. Velocity variation with grid placed 10 mm before the channel with an inlet velocity at 1 m/s.

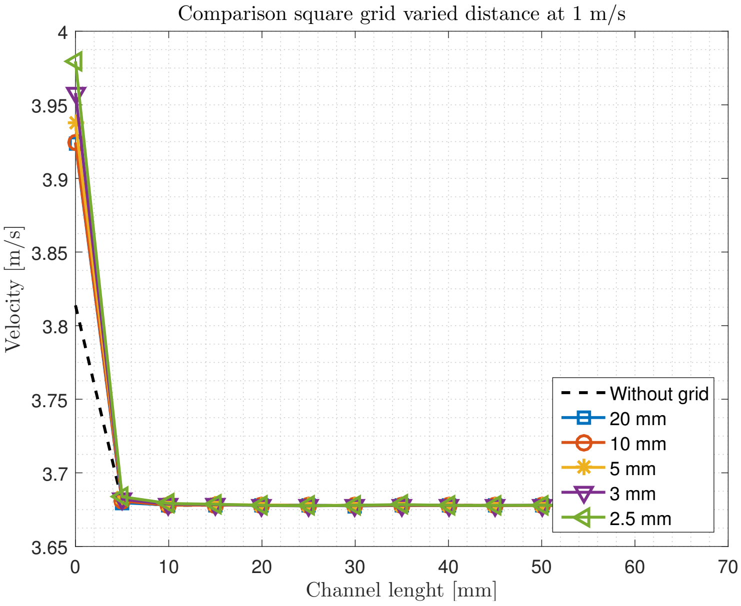

Figure 6.26. Velocity variation with square grid placed at different distances before the channel with an inlet velocity at 1 m/s.

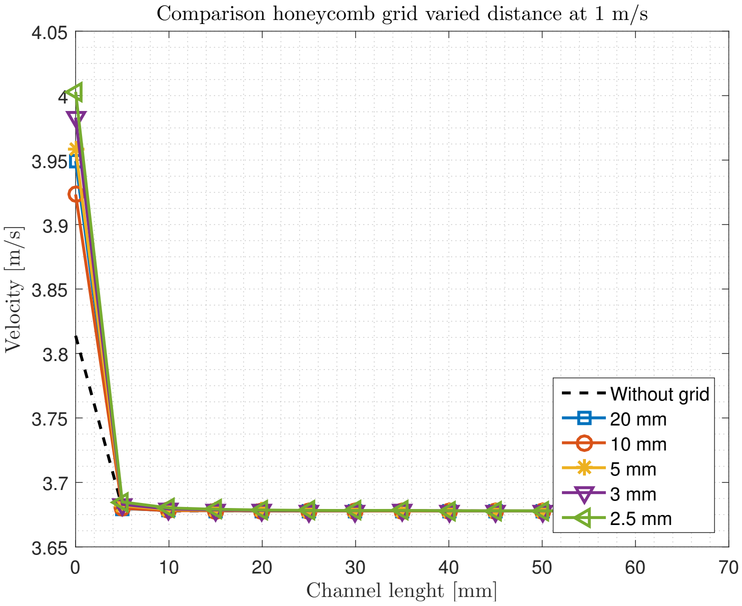

Figure 6.27. Velocity variation with honeycomb grid placed at different distances before the channel with an inlet velocity at 1 m/s.

6.8.3 Maximum velocities

This section shows the results of the maximum velocities from the planes distributed along the fluid direction. The planes used covers the fluid domain and are shown in the red box of figure 6.12.

Maximum Velocities at Inlet Velocity of 0.75 m/s

The maximum velocity for the simulation with a distance of 10 mm is shown in figure 6.28 where it is evident that the maximum velocity is higher for the case without the grids in most of the channel except the inlet, where the velocities are higher for the cases with grids.

For figure 6.29 and 6.30 the same tendencies are shown, in these cases all velocities starts out higher than the reference case without grid. Along the channel length the maximum velocity increases and becomes slightly higher for the reference case.

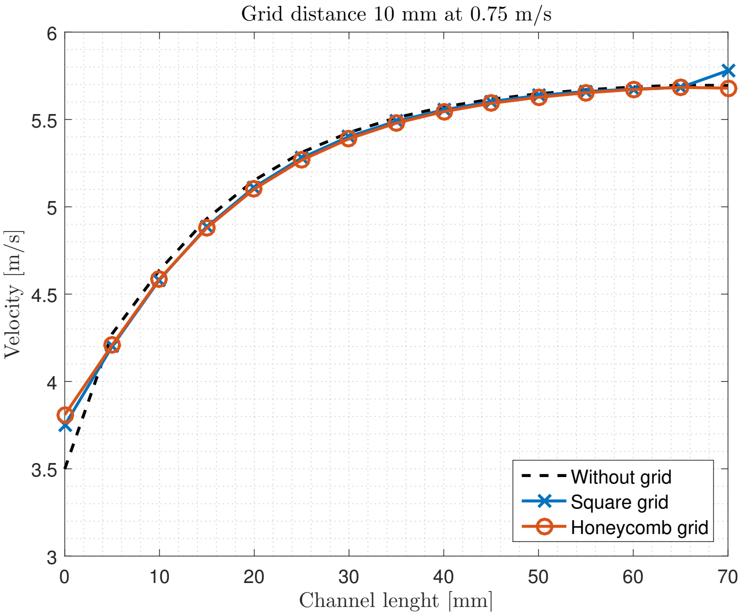

Figure 6.28. Maximum velocity with grid placed 10 mm before the channel with an inlet velocity at 0.75 m/s.

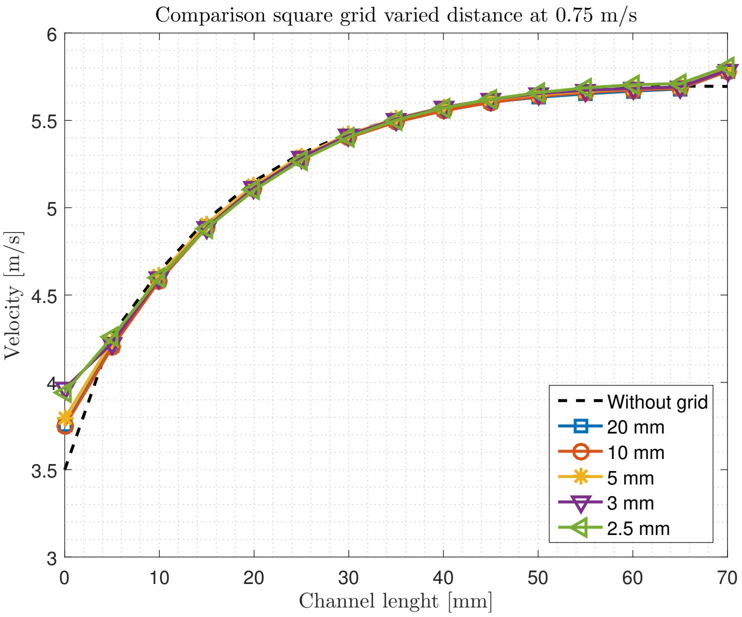

Figure 6.29. Maximum velocity variation with square grid placed at different distances before the channel with an inlet velocity at 0.75 m/s.

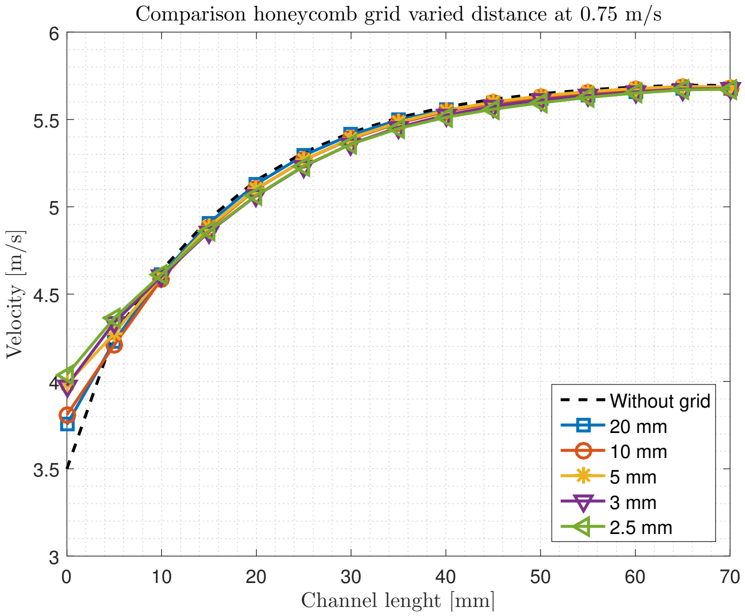

Figure 6.30. Maximum velocity variation with honeycomb grid placed at different distances before the channel with an inlet velocity at 0.75 m/s.

Maximum Velocities at Inlet Velocity of 1 m/s

The same tendencies are seen in figures 6.31, 6.32 and 6.33. The difference in maximum velocities is higher in this case indicating a stronger effect of the grid.

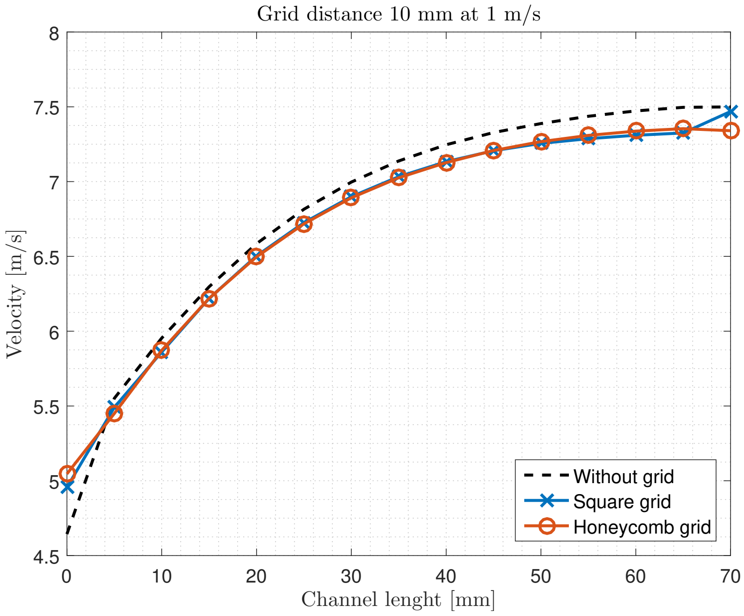

Figure 6.31. Maximum velocity with grid placed 10 mm before the channel with an inlet velocity at 1 m/s.

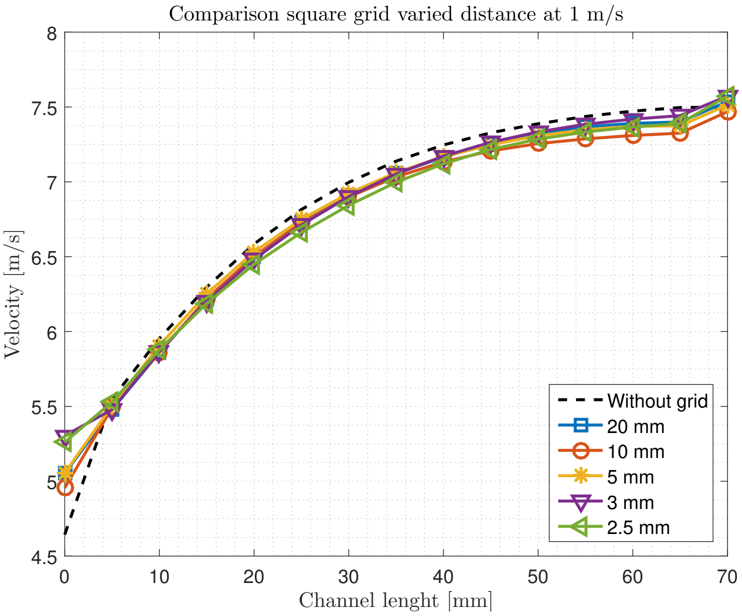

Figure 6.32. Maximum velocity variation with square grid placed at different distances before the channel with an inlet velocity at 1 m/s.

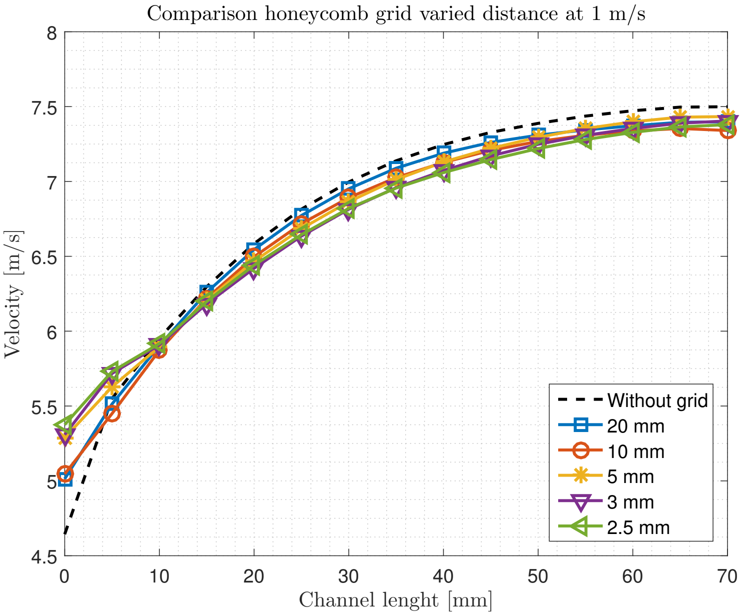

Figure 6.33. Maximum velocity variation with honeycomb grid placed at different distances before the channel with an inlet velocity at 1 m/s.

6.8.4 Turbulence Intensity

The turbulence intensity presented here will cover the distance before and right after the grid as well as inside the channel. The turbulence intensity inside the channel is obtained by taking the area average of the turbulence intensity in the planes covering the fluid domain. These planes are shown in the red box in figure 6.12. The turbulence intensities before the channel are obtained in planes as shown outside the boxes in figure 6.12, the number of planes start from the one closest to the inlet boundary condition. The number of planes used varies with the distance between the grid and channel inlet.

Turbulence Intensities at 0.75 m/s

The turbulence intensity in figure 6.34 shows that implementation of the grids increases the turbulence intensity of the flow inside the channel. As expected from the temperature results it is seen that the square grid appears to have the highest effect. At the inlet the turbulence intensity for the square gris case is almost twice as high as for the case without the grid.

A comparison of the turbulence intensity with varying distances between the square grid and channel is shown in figure 6.35. It is seen that the case with highest turbulence intensity is with 5 mm distance. The case with 2.5 mm has a higher turbulence intensity than the case without grid in the inlet of the channel, hereafter it decreases to below the level of the reference case without grid.

A similar plot for the honeycomb grid is shown in figure 6.36 where it is seen that the case with 10 mm distance has the highest inlet value at approximately 0.0375 compared to the 0.02 of the case without grid. The tendencies in the honeycomb case is different from the square grid, in the honeycomb case it is seen that all cases ends up with lower turbulence intensity than the case without grid. The cases with 2.5 mm and 3 mm are lower than the case throughout the whole channel length.

From all the figures showing turbulence intensity inside the channel it is shown that the tendency is a high turbulence intensity in the very inlet of the channel where after it decreases until about 20 mm inside the channel. This could be an effect of the entrance length which for laminar flow can be calculated as [Frank P. Incropera and Lavine., 2011]:

$$L = 0.05 \cdot Re \cdot D_h$$

The calculated entrance length for the channel is 19.63 mm which corresponds to the length where the turbulence intensity begins to increase again.

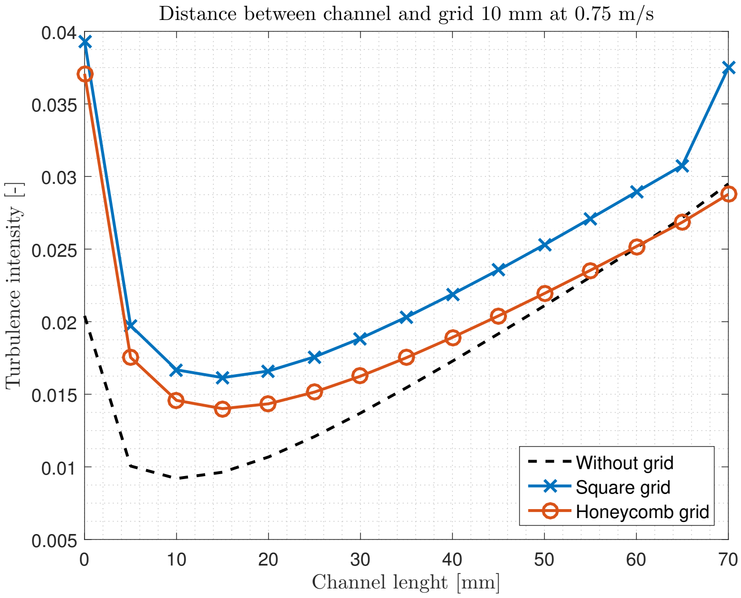

Figure 6.34. Turbulence intensity inside the channel with grids placed 10 mm before the channel and an inlet velocity of 0.75 m/s.

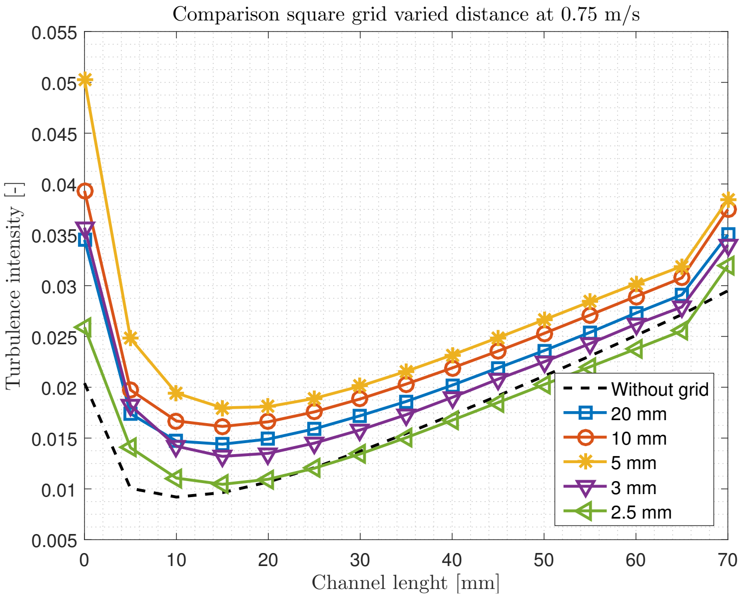

Figure 6.35. Turbulence intensity variation inside the channel with square grid placed at different distances before the channel with an inlet velocity of 0.75 m/s.

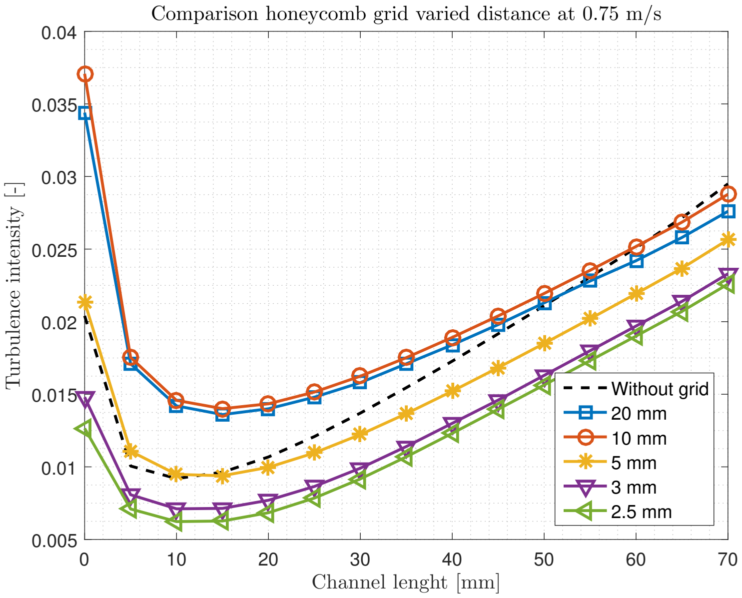

Figure 6.36. Turbulence intensity variation inside the channel with honeycomb grid placed at different distances before the channel with an inlet velocity of 0.75 m/s.

The turbulence intensities before the channel are shown in figure 6.37 and 6.38 in these plots 10 on the x-axis corresponds to the grid inlet and 11 corresponds to the grid outlet. From figure 6.37 it is seen that the 5 mm case where the intensity was highest in the channel also has the highest turbulence intensity before the channel. Figure 6.38 for the honeycomb grid shows that the two cases 2.5 mm and 3 mm which had turbulence intensities below the no grid case inside the channel also has the same tendencies before the channel.

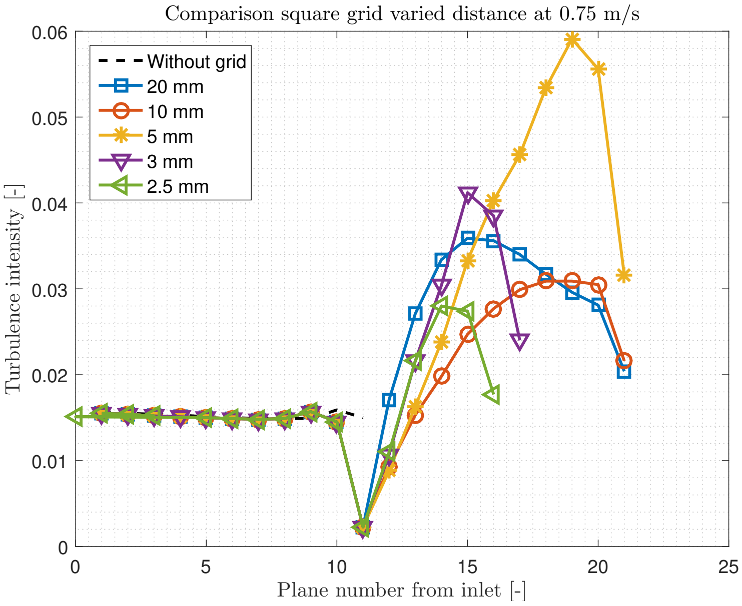

Figure 6.37. Turbulence intensity variation before the channel with square grid placed at different distances before the channel with an inlet velocity of 0.75 m/s.

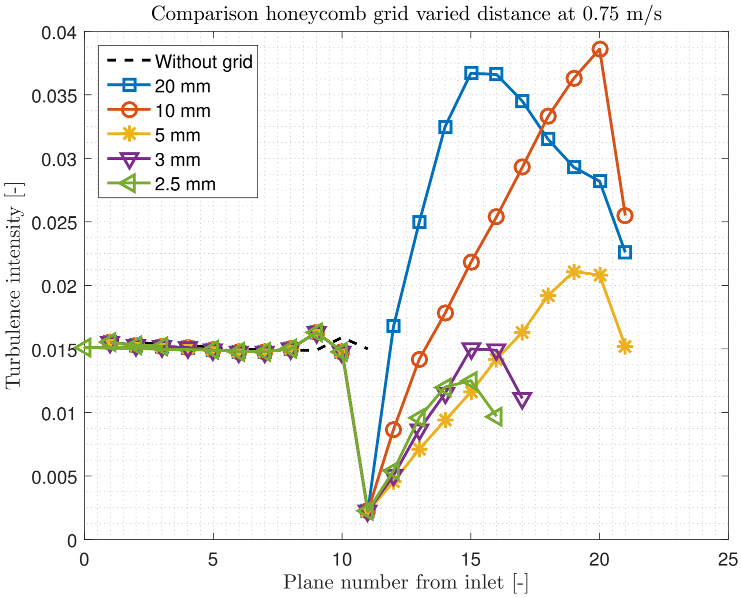

Figure 6.38. Turbulence intensity variation before the channel with honeycomb grid placed at different distances before the channel with an inlet velocity of 0.75 m/s.

Turbulence Intensities at 1 m/s

Figure 6.39 shows the turbulence intensity for the simulations with 10 mm distance, the inlet turbulence intensity increases from 0.04 for the no grid case to 0.16 with the square grid case. With an inlet velocity of 1 m/s the square grid has the highest turbulence intensity as it was the case also with the low velocity simulations.

Figure 6.40 shows the results for the square grid with different distances the tendencies are similar to the low velocity case except that for this 1 m/s simulation the 10 mm case has the highest turbulence intensity.

Figure 6.41 shows the plots for the honeycomb case. With this velocity all the cases are above the case without grid along the channel length. The case with 2.5 mm distance reaches the level of the reference case at the outlet.

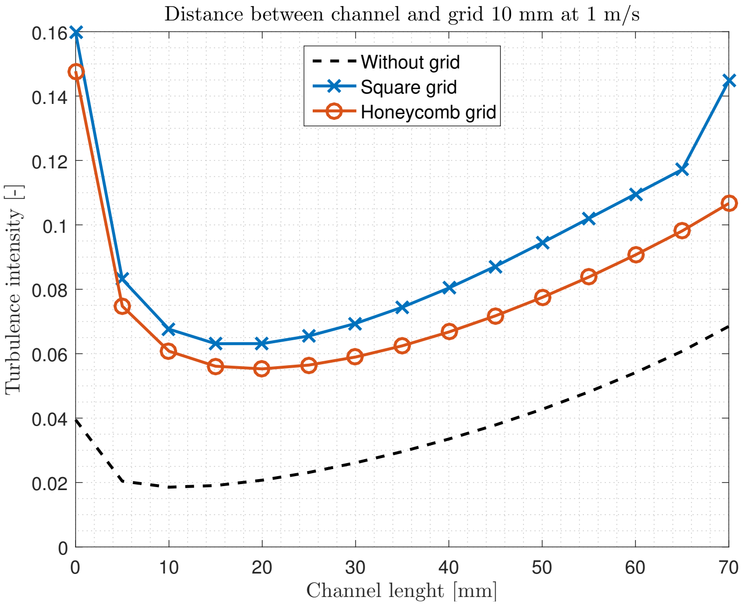

Figure 6.39. Turbulence intensity inside the channel with grids placed 10 mm before the channel and an inlet velocity of 1 m/s.

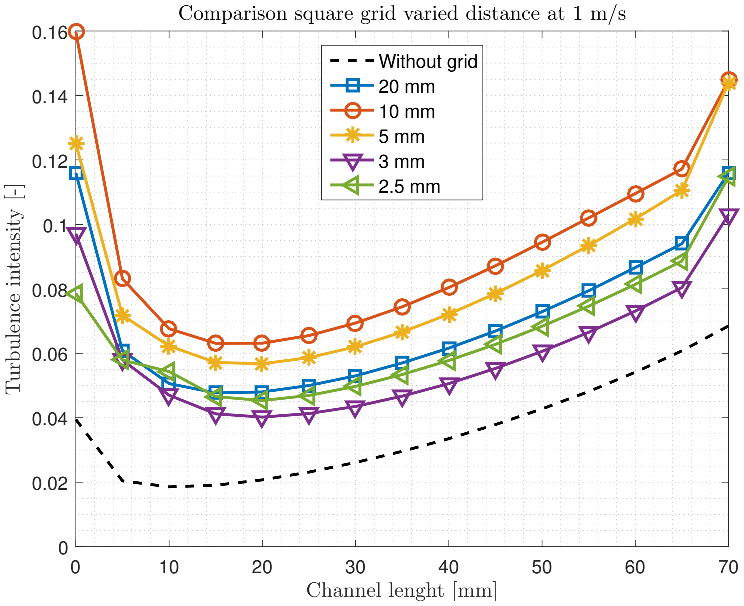

Figure 6.40. Turbulence intensity variation inside the channel with square grid placed at different distances before the channel with an inlet velocity of 1 m/s.

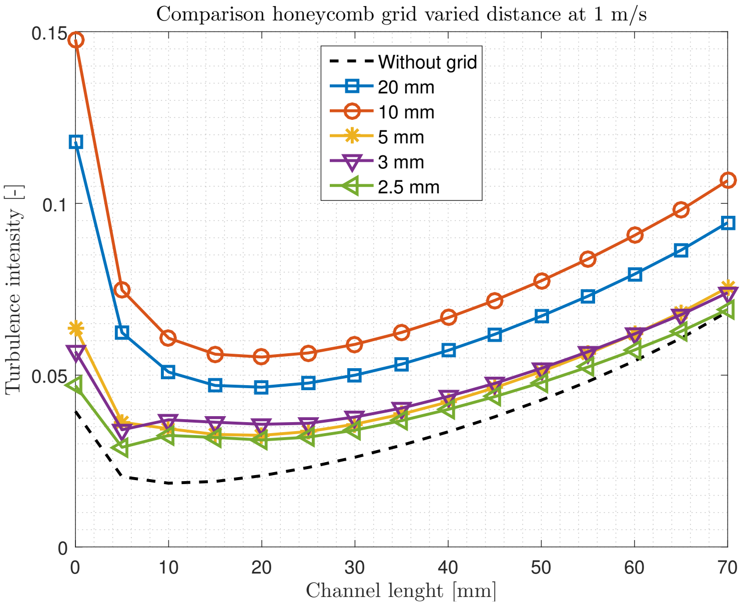

Figure 6.41. Turbulence intensity variation inside the channel with honeycomb grid placed at different distances before the channel with an inlet velocity of 1 m/s.

The turbulence intensity before the channel is shown in figure 6.42 and 6.43 where the square grid shows high turbulence intensity. For the 20 mm, 10 mm and 5 mm a high level of turbulence intensity is obtained before the channel and at approximately equal maximum value. The honeycomb grid shows high turbulence intensity for the 20 mm and 10 mm case with values a bit lower than the square grid case. The low distance cases also has lower values compared to the square grid case.

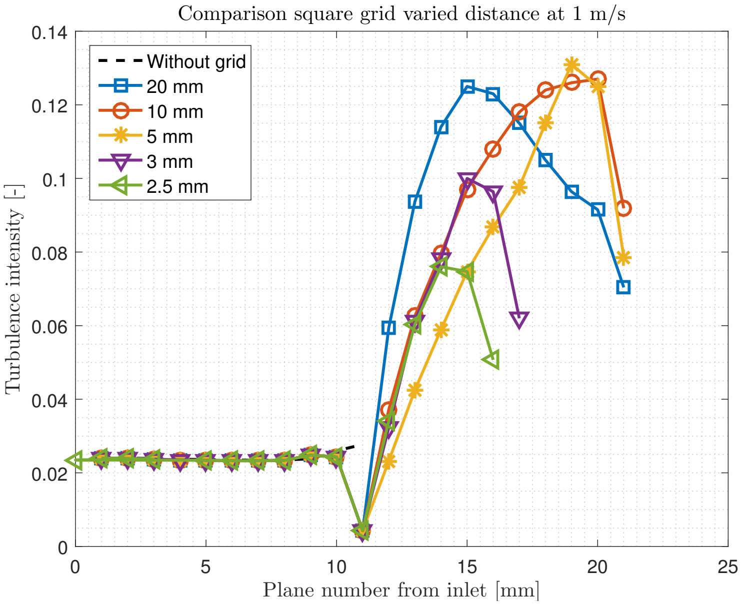

Figure 6.42. Turbulence intensity variation before the channel with square grid placed at different distances before the channel with an inlet velocity of 1 m/s.

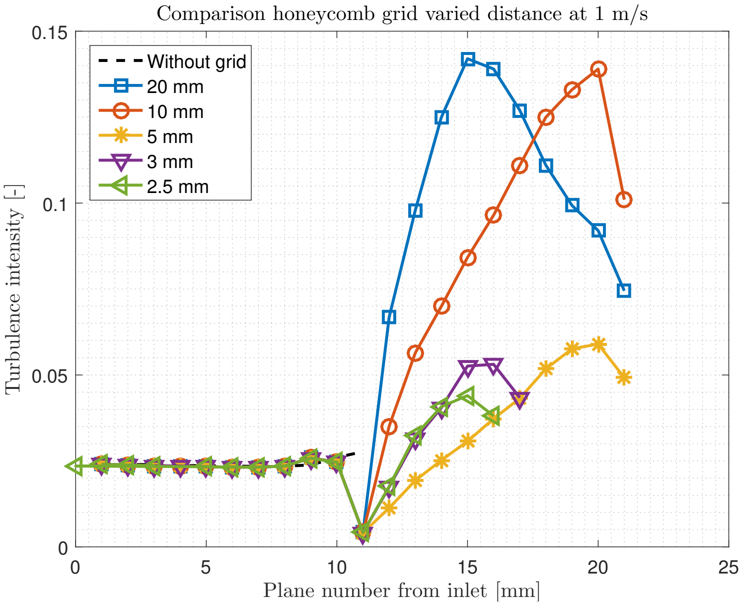

Figure 6.43. Turbulence intensity variation before the channel with honeycomb grid placed at different distances before the channel with an inlet velocity of 1 m/s.

6.8.5 Nusselt Number

In heat transfer, the Nusselt number is the ratio of convection to conduction across a given fluid layer [Çengel, 2011]:

$$Nu = \frac{\dot{q}_{conv}}{\dot{q}_{cond}} = \frac{HTC \cdot \Delta T}{\frac{k \cdot \Delta T}{L}} = \frac{h \cdot L}{k} \tag{6.24}$$

where k is thermal conductivity, h is the heat transfer coefficient, L is the characteristic length and ΔT is the temperature difference. A large Nu number indicates more effective convection and a Nu number of 1 for a fluid layer represents heat transfer across that layer by conduction only.

The Nusselt (Nu) number presented here is the "Surface Nusselt Number" directly calculated by CFD-Post where equation 6.24 becomes [ANSYS, 2018b]:

$$Nu = \frac{HTC_{eff} \cdot L_{ref}}{k} \tag{6.25}$$

where L_{ref} is a reference length specified by the user, in this case the hydraulic diameter of the channel is used. h_{eff} is defined as [ANSYS, 2018b]:

$$HTC_{eff} = \frac{\dot{q}}{T_{wall} - T_{ref}} \tag{6.26}$$

Where $\dot{q}$ is the heat flux, T_{wall} is the wall temperature and T_{ref} is a constant reference temperature specified by the user. For these calculations a reference temperature of $T_{ref} = 300K$ was chosen as a representative value for all simulations.

The nusselt numbers are exported on the interface between GDL and channel. The values are then averaged on constant z-coordinates.

Nusselt number at 0.75 m/s

The Nusselt number for the case with 10 mm is shown in figure 6.44 the tendencies are unexpected, since the case without grid has the highest Nusselt number in the entrance region with a value of approximately 8.5 compared to the square grid case of approximately 6.5.

Figure 6.45 and 6.46 shows the Nusselt number for varying distances for the two cases. The tendencies of these is also the opposite of what was expected since all cases with grid is below the case without grid. Another unexpected trend is the low distance grid where the highest temperature decrease was shown, has the lowest Nusselt numbers.

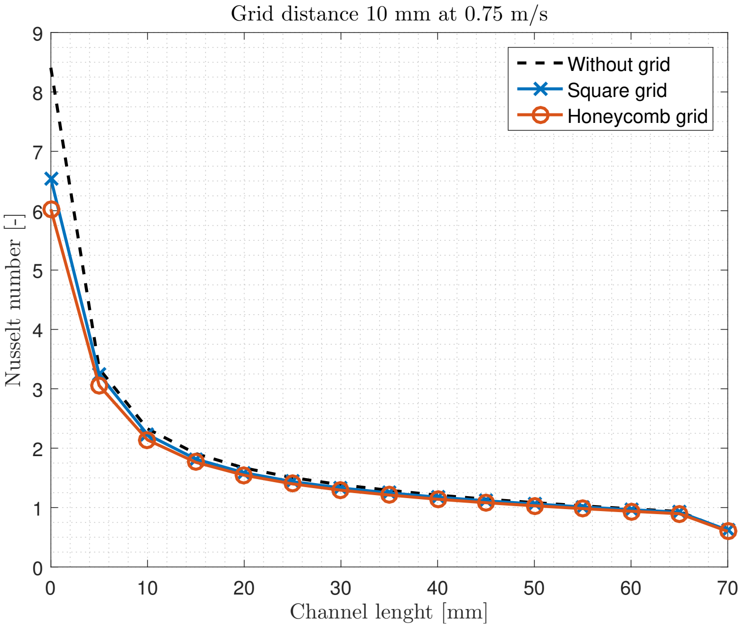

Figure 6.44. Nusselt number in the channel with the grids placed 10 mm before the channel with an inlet velocity of 0.75 m/s.

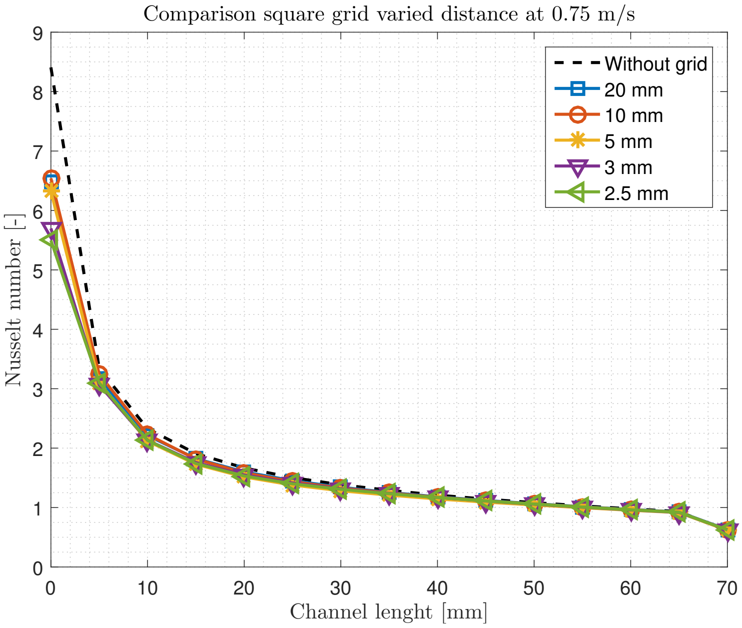

Figure 6.45. Nusselt number variation in the channel with square grid placed at different distances before the channel with an inlet velocity of 0.75 m/s.

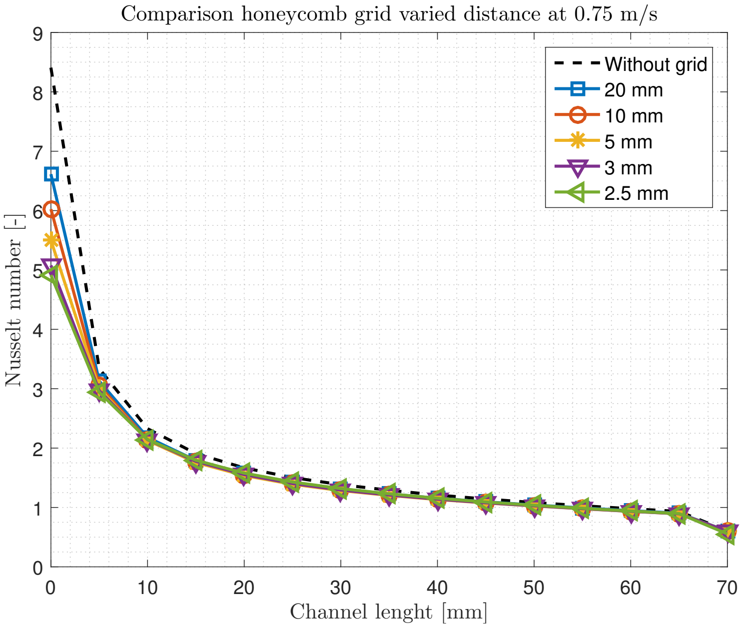

Figure 6.46. Nusselt number variation in the channel with honeycomb grid placed at different distances before the channel with an inlet velocity of 0.75 m/s.

Nusselt number at 1 m/s

The Nusselt number for the simulations with 1 m/s are shown in figures 6.47, 6.48 and 6.49 where it is seen that they follow the tendencies of the results with 0.75 m/s with an offset that yields higher values. These results also has the same unexpected tendencies as the Nusselt numbers for the 0.75 m/s simulations.

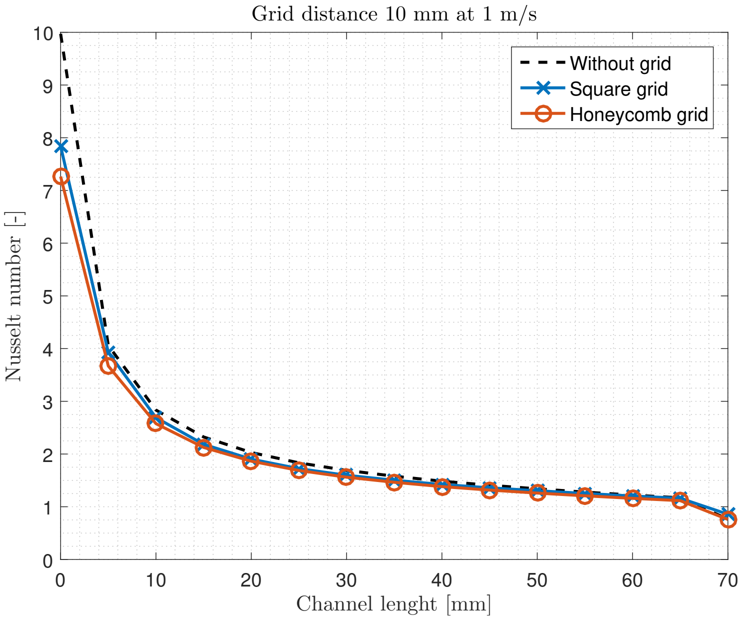

Figure 6.47. Nusselt number in the channel with the grids placed 10 mm before the channel with an inlet velocity of 1 m/s.

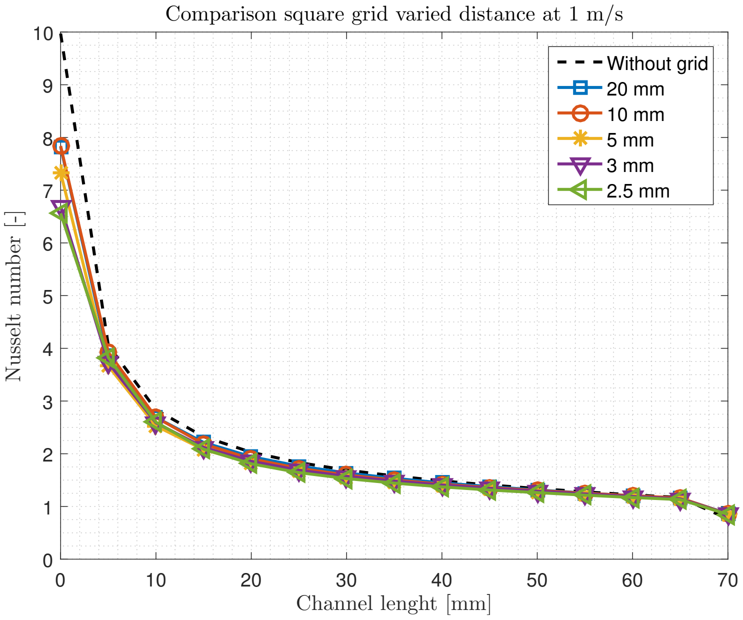

Figure 6.48. Nusselt number variation in the channel with square grid placed at different distances before the channel with an inlet velocity of 1 m/s.

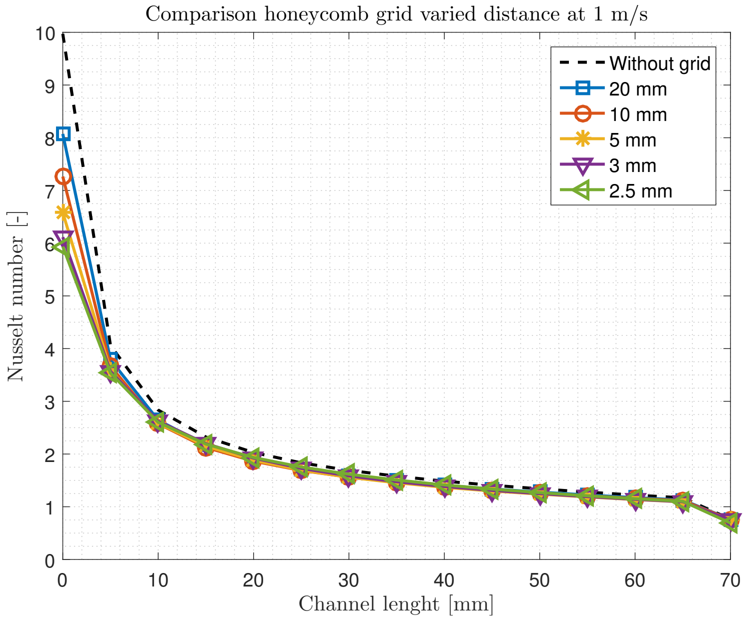

Figure 6.49. Nusselt number variation in the channel with honeycomb grid placed at different distances before the channel with an inlet velocity of 1 m/s.

6.9 Contour plots

In this section the contour plots for velocity distribution, turbulence intensity and temperature are depicted for the case with no grid and for the case with square grid at 10 mm and honeycomb grid respectively.

6.9.1 No grid case

The contour plot for the case with no grid in figure 6.50 shows the temperature distribution along the channel. It is seen that the temperature at the entrance region and further than that has a lower temperature and increases along the channel.

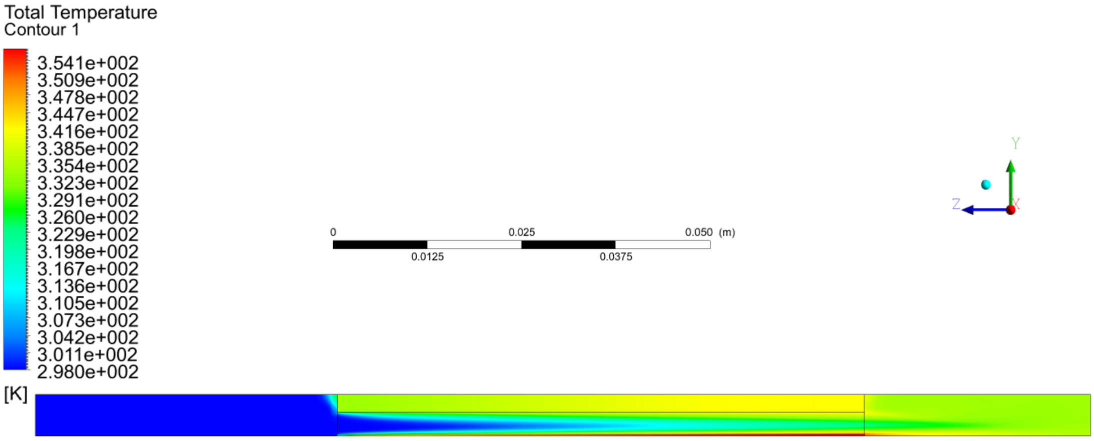

Figure 6.50. Temperature distribution in the channel

Figure 6.51 shows velocity distribution along the channel. It is seen that the velocity before the channel is in a range of 0.1 m/second whereas in the channel it gradually increasing at the entrance region up to 5 m/s where is remains constant.

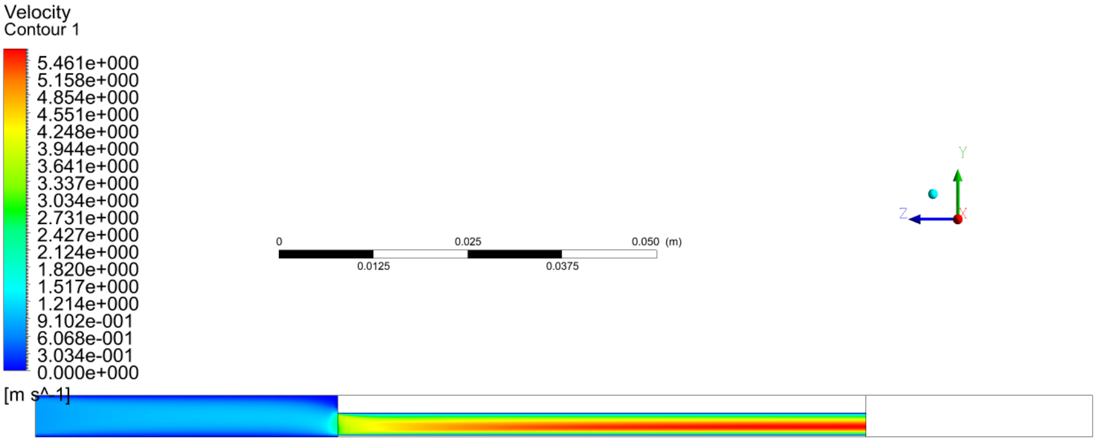

Figure 6.51. Velocity distribution in the channel

The turbulence intensity depicted in figure 6.52 show clearly that the turbulences decreases at the inlet of the channel and increases slowly in the middle of channel again.

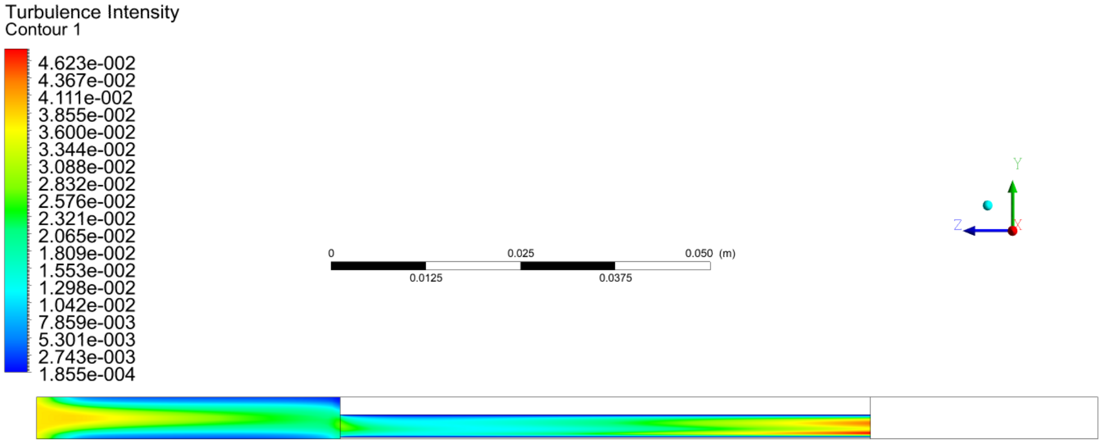

Figure 6.52. Turbulence intensity distribution in the channel

6.9.2 Square grid at 10 mm case

Figure 6.53 shows the temperature distribution for the case with square grid at 10 mm. The temperature distribution along the are more or less identical to the one with no grid.

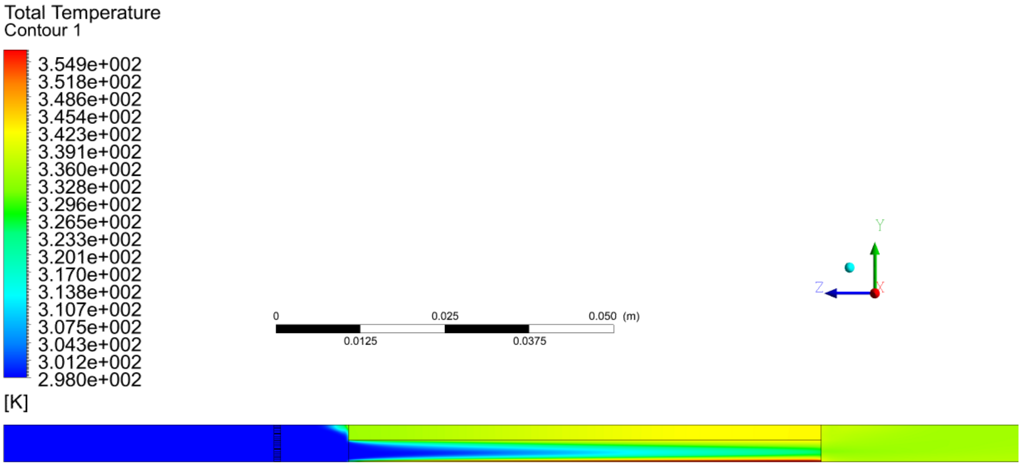

Figure 6.53. Temperature distribution in the channel

Figure 6.54 shows the velocity distribution in through the grid and along the channel. It is clearly seen that the velocity is increasing by passing the turbulence grid. The velocity increases along the channel at the entrance region and remains constant afterwards.

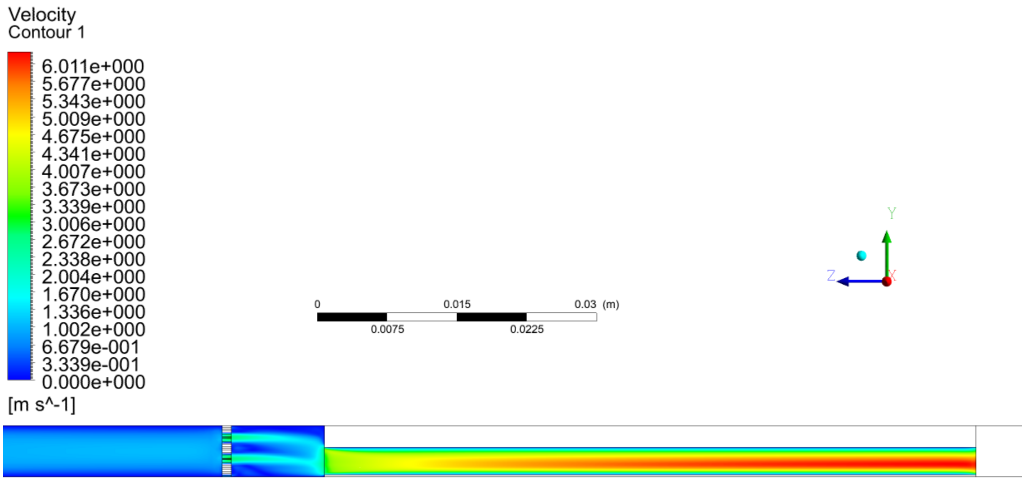

Figure 6.54. Velocity distribution in the channel

The turbulence intensity depicted in figure 6.55 shows clearly that the turbulence intensity is increased after the grid. The turbulence intensity is also higher at the inlet of the channel and makes a slight decrease and then increases again along the channel.

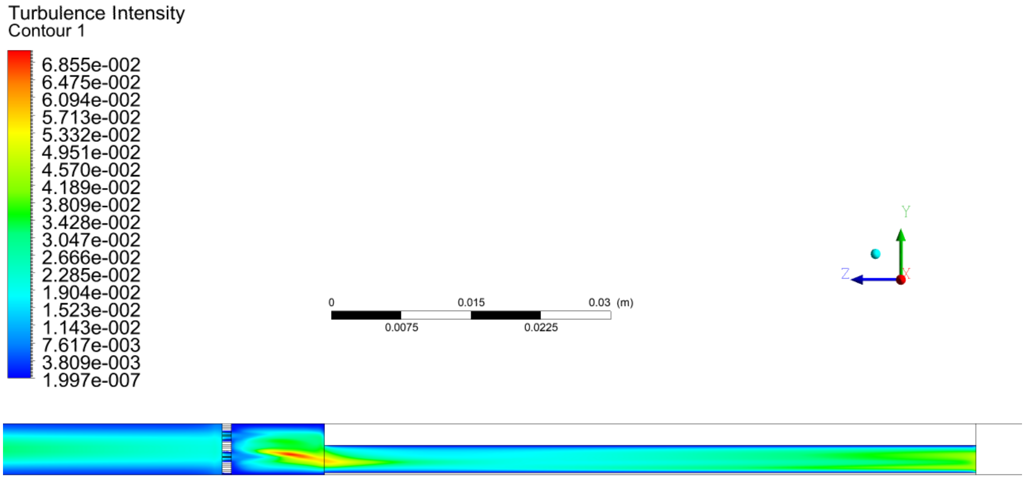

Figure 6.55. Turbulence intensity distribution in the channel

Chapter

7 Experiment

In this chapter the experimental work will be introduced with air-cooled PEM fuel cell stack in the lab. Throughout the chapter the experimental setup will be described and thereby analysis of the obtained results and the error and uncertainties within the experiment will be discussed.

7.1 Experimental Setup

In the experiment a Ballard air-cooled fuel cell stack 1020ACS (Ballard Power systems, Canada) was used.

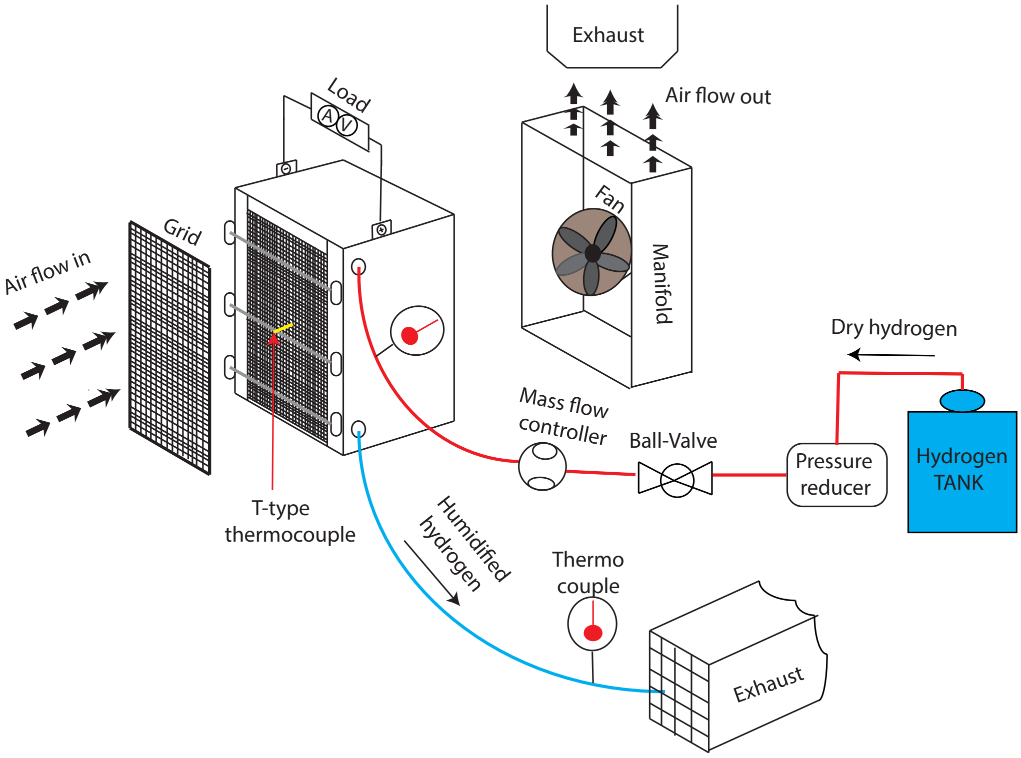

Figure 7.1. Real PEM fuel cell stack utilized in experiment

The fuel cell stack consisted of 28 cells connected in series with a cell surface area of 200 cm^2. The anode side of the stack was connected to an automated fuel cell testing station (FCATS G60, Greenlight Innovation, Canada) in order to supply dry hydrogen. Air was supplied to the cathode open channels at room temperature by a suction fan (ebmpapste 165X51 mm, 24 VDC, Hungary) that was placed behind the fuel cell stack. The suction fan was running at a constant power of 34 W. The nominal stack temperature was measured by inserting a T-type thermocouple 2.5 cm inside an air channel at the centre of the stack, see figure 7.1.

Two turbulence grids (3D printed) with dimensions of 143 mm × 157 mm was positioned 10 mm in front of the stack covering all the channels. The grid was 3D printed with rims that could be fitted inside the 3D printed frame, see figure 7.2.

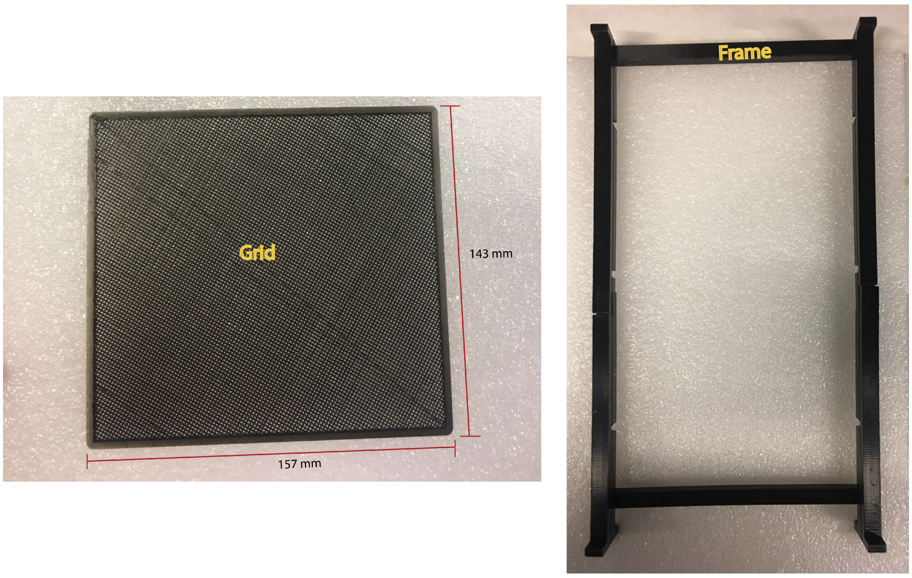

Figure 7.2. A 3D printed turbulence grid on the left side and frame for the experiment on the right side.

The frame was designed in several parts, and fitted together in order to mount the grid on the stack, see figure 7.2.

7.2 Experimental Procedure

The experiment was conducted in two parts. In the first part the grid was not mounted and the test was running without it. In the second part the grids were mounted and positioned at a distance of 10 mm before the cathode inlet. Figure 7.3 shows the experiment part 2 where the frame and grid are mounted on the fuel cell stack. In order to ensure that all the flow were directed into the grid and channels, the gaps between the frame parts and the stack were sealed with tape.

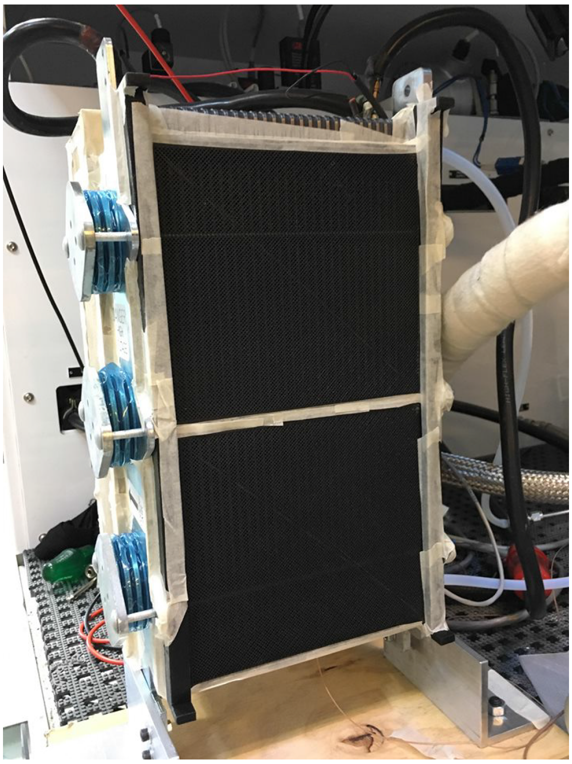

Figure 7.3. PEM fuel cell with frame and grid mounted

Dry hydrogen was supplied to the anode side with stoichiometry of 1.3 and the air was supplied to the cathode channels of the stack. The load was then applied on the stack with a script running from 0 A to 45 A in steps increasing with 5 A for every step. Each step was run at an interval of 20 min. This was done to ensure the stabilization of the voltage and temperature. At each step when the current increases the voltage decreases continuously until it reaches steady state. The fans rotational speed was kept constant with a constant power of 34 W.

All the data were measured using FCATS G60 fuel cell test station and they were saved and processed using the integrated LabView software for the FCATS G60. When the experiments was running after all initializing steps, the setup was tested for hydrogen leak using a hydrogen sensor in order to ensure that there was no leak and that everything was working properly. In the fuel cell lab there is no air conditioning system to ensure constant room temperature. The test stations are connected to an exhaust device which is connected to the outside. This means that the room temperature is affected by the outdoor temperature. And as the measurements are dependent on temperature and humidity of the environment all tests were conducted at 3 different times. All the data were then collected and then averaged.

7.3 Experimental Results

In this section the experimental results will be analyzed and presented.

The experiments conducted in this study includes two different grid types: A square grid and a honeycomb grid. The experiments were performed on different fuel cell stacks as the first stack leaked hydrogen and was replaced with another stack. Furthermore the distance between the turbulence grid and the fuel cell stack was located at the same locations before the cathode inlet for both honeycomb grid and square grid. Turbulence's generated by a grid starts at certain distance behind the grid and then dissipates again [Torsten Berning and Shakhshir, 2018]. Thus placing the grid close to cathode inlet will carry the turbulence deeper into the channels. Because of the practical issues regarding placement of the turbulence grid, the chosen location were 10 mm. The metal rods holding the fuel cell stack, which is depicted in figure 7.1, introduced some difficulties regarding installation of the turbulence grid and therefore the grid was placed outside the metal rods with a minimum distance of 10 mm from the cathode inlet. In the next section all the experimental results will be analyzed and depicted.

7.3.1 Honeycomb Grid

The first experiment was conducted with honeycomb grid. The measured values are the power output, cathode inlet temperature and the cell voltage. Figure 7.4 shows the polarization curve for the case with honeycomb grid and no grid respectively. From the figure it is seen that the best performance is achieved for the case with honeycomb grid. The maximum achievable power for the case with honeycomb grid is 544.6 W whereas for the case with no grid it is 530 W. This implies that the honeycomb grid has increased the performance by 2.75 %. By that it can be stated that the turbulence grid indeed increases the performance of the fuel cell which could be due to induced turbulence to the cathode channels.

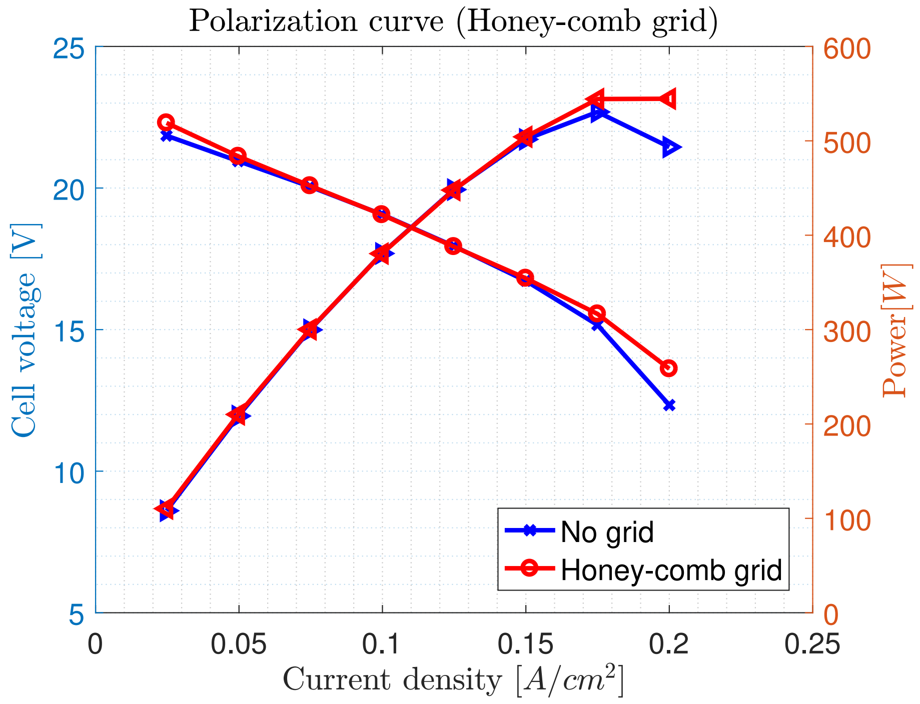

Figure 7.4. Polarization curve for the case with honeycomb grid and no grid

Examining the cathode inlet temperature on figure 7.5 it is seen that for the case with grid, the temperature is a bit lower compared to the case with no grid. The cathode inlet temperature for the case with grid reaches 40.08 °C while for the case with no grid it reaches 40.69 °C respectively. This implies that the grid introduces a more effective cooling.

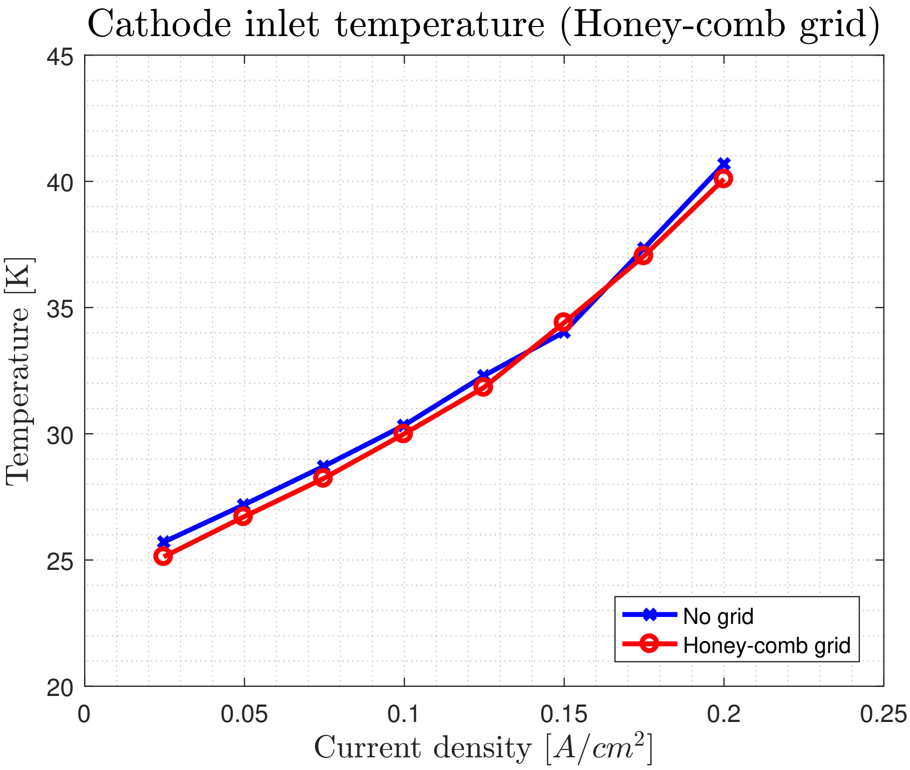

Figure 7.5. Cathode inlet temperature for the case with honeycomb grid and no grid

7.3.2 Square Grid

The experiment conducted with the square grid was performed on a different fuel cell stack than the one used for testing the honeycomb grid due to leak of hydrogen.

Figure 7.6 shows the performance of the turbulence square grid. It is clearly observed that the square grid increases the performance of the fuel cell compared to the case with no grid. This indicates that turbulences are induced by the grid and by that resulting in better performance. The aim of turbulences is to provide effective cooling by disturbing the thermal boundary layer in the fuel cell channels. Examining the performance curve on figure 7.6 the maximum power for the case with square grid is 778.47 W while for the case with no grid is 705 W and thus the performance of the fuel cell with the square grid has increased with 10.42 %.

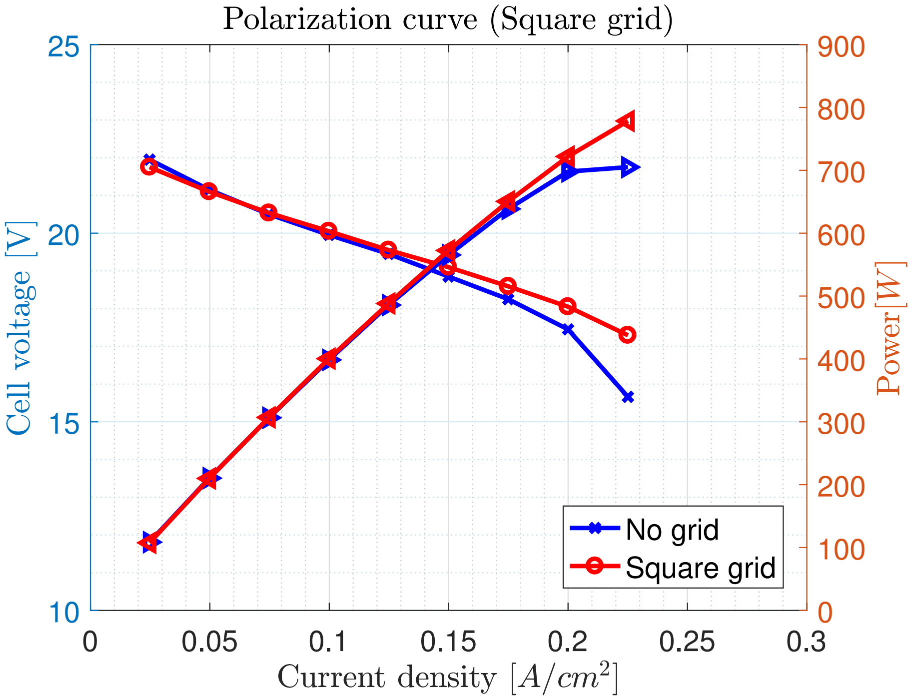

Figure 7.6. Polarization comparison curve for the case with square grid and no grid.

Observing the voltage for the case with no grid, it decreases rapidly at current density of 0.2 A/cm^2. This implies that the maximum operating current is reached otherwise the performance will decrease and produce more waste heat. Generally the voltage at each current density starting from 0.1 A/cm^2 for the case with no grid is lower. Evaluating the case with the square grid the power curve has not reached its peak point and thus it is believed that the performance could be increased even further e.g. operating at even higher current densities.

Figure7.7 shows clearly an indication that experiment conducted with no grid started at a lower room temperature. The cathode inlet temperature for the case of no grid reached higher temperatures compared to the case with grid. At current density of 0.175 A/cm^2 the temperature starts to increase rapidly and reaches a temperature of 42 °C at maximum power. Observing the cathode inlet temperature for the case with grid, the curve seems to have a almost constant slope. Furthermore, the temperature with grid is lower than that of the case with no grid, the temperature with grid is 38.9 °C. Examining the temperatures for the case with no grid and with the grid respectively, it can be stated that the turbulence square grid indeed results in more effective cooling and higher performances.

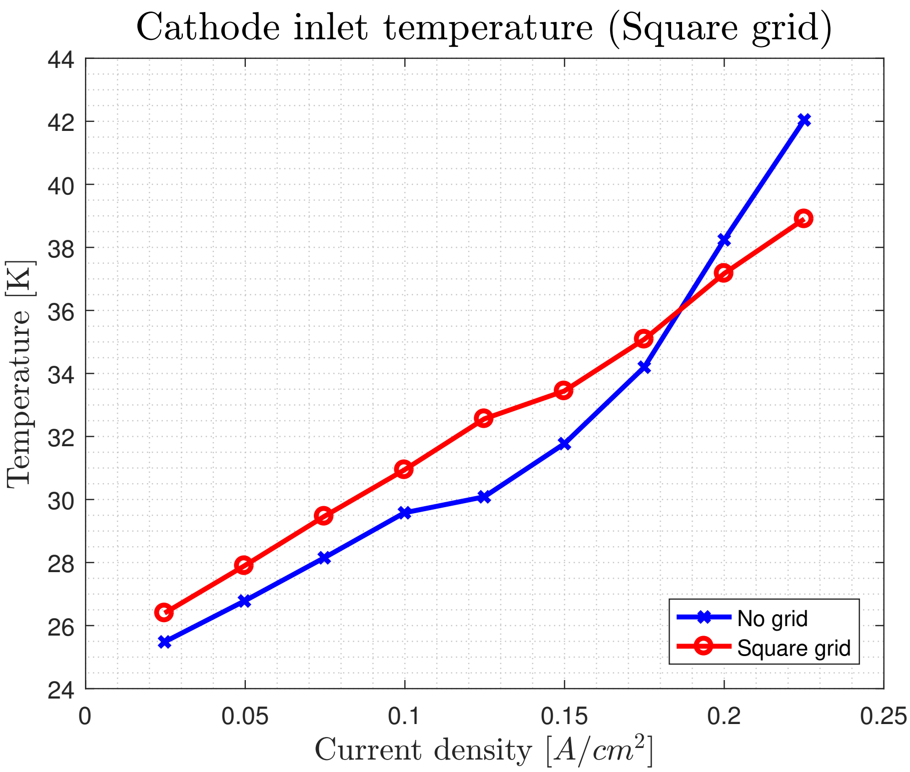

Figure 7.7. Cathode inlet temperature for the case with square grid and no grid

Generally it has been proven experimentally that the turbulence grid induces turbulence which leads to higher performance for the PEM fuel cell stack. In both cases with the two different grids mounted on the fuel cell stack the performance has been improved.

7.4 Error Sources

The experiment were followed by uncertainties and error sources. Overall it must be stated that the metal rods holding the PEM fuel cell stack might possibly have affected the results. The turbulences might have been affected by the metal rods in the regions behind the metal rods. The metal rods might have provided a shielding effect for the case with 10 mm

The room temperature might have caused a possible error as well. There's no ventilation system in the fuel cell lab but an exhaust device connected to the outdoor. This means that the room temperature in the fuel cell lab is dependent on the outdoor temperature. The duration of each experiment was approximately 4 hours. Within 4 hours the room temperature changes with couple of degrees which indeed affects the results. Higher room temperatures leads to lower performance as the air temperature increases.

The gap between the frame and the fuel cell stack might have caused to a lower performance. The air near the edges and corner might have been affected by the gap between the stack and the frame. Even though there were sealed in order to ensure that no air was leaked through the gaps. If the air leaked through the gaps it could lead to less flow in the edges and corners of the turbulence grid and less airflow in these regions might lowers the overall performance of the fuel cell stack.

Degraded fuel cell stack might possibly have affected the obtained data for the experiment conducted with honeycomb grid. The performance of the fuel cell was generally low to begin with and by placing turbulence grid it could be forced to operate at higher currents, meaning it could provide more power output.

Chapter

8 Discussion

In this chapter the obtained results from the CFD models and experiments will be compared and discussed. Hence the only achievable results from the experiment conducted was the case with grid positioned 10 mm distance from the cathode inlet, the main focus in this chapter will rely on the simulation conducted at that particular case.

8.1 Constant Air Properties

In this study a mistaken was found at the very end of the submission. The simulation were conducted at constant density which shouldn't be the case. The air properties as default are set to constant in ANSYS FLUENT. This means that the density and specific heat capacity were constant throughout the fluid domain. A quick study was made for the case with no grid and square grid at 10 mm respectively. The default settings for air properties (density and specific heat capacity c_p in ANSYS fluent were changed from being constant to ideal incompressible. The new simulations showed very similar tendencies for turbulence intensity along the channel and temperature respectively. The only significant difference was found for the mean velocity along the channel which was increasing along the channel with the new simulations where it was constant for simulations at constant density. This is expected as the increase in temperature is followed by a decrease in density which leads to higher velocity.

8.2 Turbulence Intensity

In order to see whether the grids induces turbulences, turbulence intensity was determined from the model. Figure 6.37 and figure 6.38 showed that turbulence intensity increased by passing the grids. This indicates that the both grids are inducing turbulences. The square grid achieved higher turbulence intensity compared to the honeycomb grid, beside for the case with grid placed 5 mm before the cathode inlet, here the honeycomb achieved highest turbulence intensity. The turbulence intensity reached lower values as the grid was placed closer to the cathode inlet. The might be due to the fact that turbulences were not allowed to be fully developed before entering the cathode inlet. The turbulences might also have been affected by the channel walls at the inlet. As the flow hits the wall, some of the flow might have been reversed and opposed the turbulences.

The turbulence intensity in the channel depicted in figure 6.35, decreased at the entrance region and increased along the channel length afterwards. The square grid induced highest turbulence intensity in the channel followed by the honeycomb grid. The increase of turbulence intensity might be due to the increase in the maximum velocity. Figure 6.28 shows the maximum velocity in the channel. Here it is seen that the maximum velocity increases along the channel which may lead to higher turbulence level along the channel and thereby an increase in turbulent intensity. It is interesting to see that the turbulence intensity decreases in the entrance region. One reasonable explanation might be that the level of turbulences of the flow is high right before the cathode inlet. When the flow enters the cathode channel, the level of turbulences decays due to reduction of area but also the flow gets more directed. And as the flow starts to develop along the channel the turbulence intensity increases again.

8.3 Temperatures

The average fluid temperatures depicted in 6.13 was found to be the same for all three cases: No grid, square grid at 10 mm and honeycomb grid at 10 mm. The inlet velocity was set to be 0.75 m/s. The temperature difference between the cases were only 0.1 K. In all cases, area-weighted average of the temperature where determined in planes along the channel. The planes covered only the fluid domain. The average temperatures in fig.6.14 with the same cases but area-weighted averaged in the planes covering the entire channel domain (including the walls), showed a decrease in average temperature for the cases with the grids. The highest temperature was found with the case with no grid. For the case with grids, the square grid achieved lowest temperature along the channel followed by the honeycomb grid. The outlet temperature for the case without the grid was determined to be 341.06 K, 340.35 K and 340.94 K for square and honeycomb grid respectively. The square grid induces higher turbulent intensity and this might lead to higher heat transfer in the cathode channel followed by the honeycomb grid. The turbulences might disturb the thermal boundary layers and thus increase the heat transfer.

Figure 6.16 is the extended version of figure 6.14 but with only square grid. The square grid were positioned at several distances before the cathode inlet. The average temperature was found to decrease as the grid were placed closer to the cathode channel. Previously the study showed that the turbulence intensity might disturb the thermal boundary layer and thereby increase the heat transfer in the channel. Figure 6.37 shows turbulence intensity in the channels for the case with square grid placed at different distances before the cathode inlet. It was found from the figure that the turbulence intensity in the channel decreased as the grid was placed closer at the cathode inlet and so the temperature. This might seem as a contradiction to the statement that higher turbulence intensity leads to higher heat transfer in the channel and thereby reduces the temperature even further. The lower wall temperature for the cases were the grid is placed closer to the cathode inlet might be due to the accelerated flow from the grid directed to the cathode front walls. Here the heat transfer might be very high due to higher temperature difference between the walls and the fluid domain and because of the high velocity accelerating from the grid which then leads to a lower wall temperature of the channel in general. As the Nu number is a function of Re number a higher velocity corresponds to a higher heat transfer. The same tendencies is seen for the cases with honeycomb grid.

Increasing the velocity resulted in higher temperature differences between the case without grid and the cases with grids. This is because the grid induces more turbulence and thereby the overall turbulence level increases in the channels with the cases for the grids.

The experiment also showed a temperature decrease at the cathode inlet with the square grid in comparison to the case without grid. And here cathode inlet temperature was lower for the square grid followed by honeycomb grid. This again might be due to the turbulences introduced by the grid.

8.4 Nusselt Number

The previous mentioned results indicated that the turbulence grids induces turbulences and thereby a lower channel wall temperature was obtained as the turbulences level increased along the channel. All this indicates that turbulence grid increases the heat transfer in the channels by introducing turbulences and disturbing the thermal boundary layer thickness but fig.6.44 showed contradicting results. Here the Nu number was found to be higher for the case without grid. Examining the heat flux and the local temperature difference between the reference temperature (300 K and local wall temperature along the channel for the case with square grid at 10 mm and no grid with inlet velocity of 0.75 m/s, it is found that heat flux for the case without grid is generally higher. The Nu numbers in general shows weaker effects that expected. Previous experiments by other researchers at Energy technology have gotten results with temperature differences of several degrees.

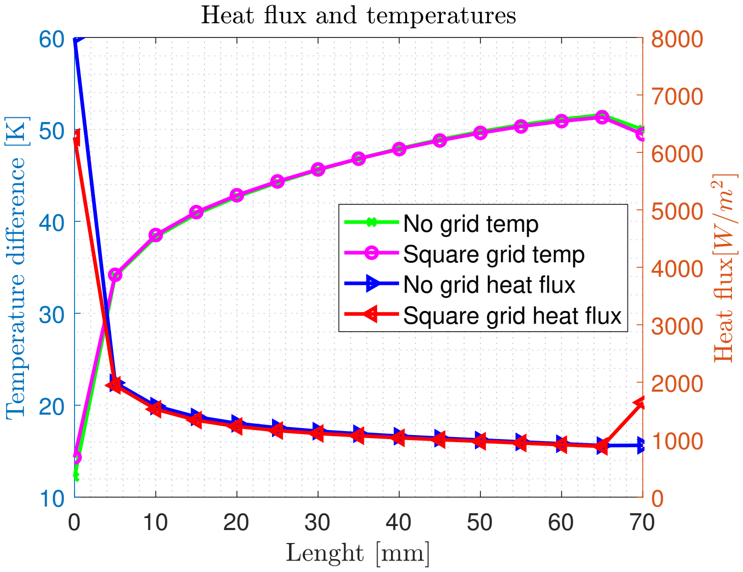

Figure 8.1. Heat flux and temperature distribution with and without the grid

As the temperature differences are almost identical, the main reason why the Nu number is higher for the case with no grid is due to the heat flux. It is seen at the inlet that the heat flux is 27 % higher. It is unclear why it behaves in such way. The mass imbalance throughout the computational domain was in a range of $2 \cdot 10^{-12}$ for all cases. The heat flux balance evaluated at the inlet and outlet were found to be the same.

8.5 Experimental Results

The fuel cell lab caused a lot of problems during the experiments. First of all the fuel cell stack utilized in the lab began to leak hydrogen out to the environment and the hydrogen alarm went off. This might be one the the reasons why the general power output in the first experiment, the case with honeycomb grid and no grid, was lower compared to the experimental results obtained for the case with square grid and no grid with a different fuel cell stack. Generally the power output for the cases with the grids were higher and the corresponding voltages were lower. The temperature were also found to be lower for the cases with the grids.

The experiment conducted with the case of square grid was found to increase the performance by roughly 10 % compared to the case without the grid. For the honeycomb grid the increased performance was 2.75 %. The experiments could be conducted at even higher current density for the case with the square grid. As it is seen in figure 7.6 the case with square grid has not reached it's peak point and thus it indicates that the power output could be even higher for that particular case and the corresponding voltage was decreasing in a stable manner.

The new ventilation system in the fuel cell lab is not properly installed and every time the experiment was conducted the alarm went off. This is why the experiments were conducted only for the cases where the grids were placed 10 mm before the cathode inlet. The purpose of the experiments were to place the grid at different distances before the cathode inlet but as the ventilation system caused the problems which made the alarm go off then it was not allowed to do more experiment before the problem was solved.

CHAPTER

9

Conclusion

The scope of this study was to investigate whether the turbulence grids induced turbulence and improved the performance of the air-cooled PEM fuel cell. CFD models were build for a single PEM fuel cell channel with and without the grids located at different distances before the cathode inlet. The model was assisted with an experimental study on a Ballard air-cooled fuel cell stack 1020ACS (Ballard Power systems, Canada). In order to investigate whether the grids induced turbulences, the turbulence intensity was determined by locating planes before and after the grids respectively. The turbulence intensity was then area-weighted averaged at each plane and the model showed that the turbulence intensity increased after the grids. This indicates that the grid induces turbulence. The square grid was found to be superior in performance by inducing turbulence both after the grid and in the channel respectively. The average wall temperature along the channel decreased by placing turbulence grids before the cathode inlet. Furthermore the temperature decreases even further by placing the grids closer to the cathode inlet while the turbulence intensity was decreasing as well with the grid at a smaller distance.

Increasing the velocity from 0.75 m/s to 1 m/s resulted in an overall increase of turbulence intensity after the grid and inside the channel. Moreover the temperature in the channel walls decreased even further.

The experimental results were conducted on two different stacks due to hydrogen leaking problems. The results proved that the turbulence grids improves the performance of the air-cooled fuel cell stack. The improved performance for the square grid was 10.42 % and 2.75 % for the honeycomb. The cathode inlet temperature for the case with square grid at maximum power was found to be 38.9 °C and 42.2 °C for the test without grid. For the honeycomb grid the temperature at maximum current density was found to be 40.08 °C and 40.69 °C for the test without grid. According to figure 7.6 the power had not reached its peak point and thus the performance could be improved even more by conducting the experiment at even higher current densities. For the case with honeycomb grid it is concluded that the low values might be due to an end of life fuel cell stack which also leaked hydrogen during the last measurements in the experiment with honeycomb grid.

The Nu number showed contradicting results in the CFD modelling. This is due to the uncertainties of the model e.g simulations were conducted with constant air properties. Moreover the electrochemical process in the channel were not modelled and a constant heat flux was applied at the bottom wall of the GDL layer whereas in the reality the heat is increasing gradually when increasing the current.

Overall the simulated results showed that the grid induces turbulence which leads to higher turbulence level in the channel as well. The wall temperature decreases by placing turbulence grids before the cathode inlet which is indicated in higher heat transfer in the channel. The experiment assisted the model by improving performance of Ballard air-cooled fuel cell stack 1020ACS (Ballard Power systems,Canada) by placing grids before the cathode inlet and furthermore resulted in a decreasing temperatures.

Chapter

10

Future work

In the future work the material properties for air such as density and specific heat capacity should be changed from being constant to ideal gas incompressible relation to temperature in the commercial ANSYS Fluent 19 program.

The CFD model could be build with implementation of the electrochemical processes inside the cathode channel. This will most likely lead to a more realistic results and might represent a more accurate effect of the turbulence grids.

Another thing that could be interesting to investigate in the future work is parametrization of the grid dimensions. This will lead to an optimal design for the grids and the cathode channel by analyzing key parameters such as rip width, grid thickness and pore size etc. The tolerance level of the 3D printers was quite high, which lead to a low accuracy of the resolution of the 3D printed grids. In the future it could be beneficial to manufacture the grids on a 3D printer with higher resolution. This would lead to higher accuracy of the grid dimensions. The used 3D-printer for this study was installed with a 0.4 mm nozzle which means that the smallest dimension possible for printing is limited by the nozzle size. Another idea instead of 3D printed grids to prove the concept could be laser cut grids.

The experimental work should be conducted by varying the grid distance at several location before the cathode channel. This will give additional understanding of an optimal grid distance by examining the performance of Ballard 1020 ACS air-cooled fuel cell. Moreover the grids could be designed with different angle placed behind each other to increase the turbulence level even further.

An investigation containing experimental and simulations of multiple grids stacked together could be interesting to see the effect on the performance as well as the temperatures.

It would be beneficial to redo the experiments with a fuel cell stack at beginning of life. Here it would be ensured that the stack was fully functional and not damaged by wrong usage.

The fan speed was kept constant throughout the experiment. This means that especially at lower current densities the operating temperature was far below the optimal temperature range as the temperature range of the Ballard 1020 ACS air-cooled fuel cell stack is between 38 °C to 70 °C. By designing a fan-speed controller such that the fan speed can be adjusted the performance might increase even further.

List of Figures

List of Tables

Bibliography

Advances in Hydrogen Production, Storage and Distribution.

ANSYS, 2018a. Inc. ANSYS. *ANSYS Meshing users guide.* ANSYS, Inc., 2018.

ANSYS, 2010. Inc. ANSYS. *ANSYS Meshing users guide.* ANSYS, Inc., 2010.

ANSYS, 2018b. Inc. ANSYS. *ANSYS Fluents User's Guide.* ANSYS, Inc., 2018.

ANSYS, 2018c. Inc. ANSYS. *ANSYS Fluents Theory Guide.* ANSYS, Inc., 2018.

AZoM, 2002. AZoM. *Graphite (C) - Classifications, Properties and Applications of Graphite.* `https://www.azom.com/article.aspx?ArticleID=1630`, 2002. Visited 2018/13/04.

Barbir, 2013. Frano Barbir. *PEM Fuel Cells Theory and practice.* Elsevir Academic Press, 2^{nd} edition, 2013. ISBN 9780123877109.

Berning and Kær, 2018. Torsten Berning and S. K Kær. *A thermodynamic analysis of air-cooled proton exchange membrane fuel cells operated in different climate regions*, 2018.

Farah et al., 06 2016. Shady Farah, Daniel Griffith Anderson and Robert S Langer. *Physical and Mechanical Properties of PLA, and their Functions in Widespread Applications - a Comprehensive Review.* 107, 2016.

Frank P. Incropera and Lavine., 2011. Theodore L. Bergman Frank P. Incropera, David P. DeWitt and Adrienne S. Lavine. *Fundamentals of Heat and Mass Transfer.* Wiley, 7^{th} edition, 2011. ISBN 978-0470501979.

Fuel Cells Etc, 2013. Fuel Cells Etc. *What is the Purpose of a Gas Diffusion Layer (GDL)?* `http://fuelcellsetc.com/2013/02/purpose-of-a-gas-diffusion-layer-gdl/`, 2013. Visited 2018/13/05.

Kaur, 2016. Gurbinder Kaur. *Solid Oxide Fuel CEll Components.* Springer, 1^{st} edition, 2016. ISBN 9783319255989.

Mikhailova et al., Sep 2005. N. P. Mikhailova, E. U. Repik and Yu. P. Sosedko. *Reynolds Number Effect on the Grid Turbulence Degeneration Law.* Fluid Dynamics, 40(5), 714–725, 2005. ISSN 1573-8507. doi: 10.1007/s10697-005-0109-1. URL `https://doi.org/10.1007/s10697-005-0109-1`.

Munson et al., 2012. Bruce R. Munson, Wade W. Huebsch and Alric P. Rothmayer. *Fundamentals of Fluid Mechanics*. John Wiley, 7^{th} edition, 2012. ISBN 9781118116135.

PRITCHARD, 2016. PHILIP J. PRITCHARD. *Introduction To Fluid Mechanics*. JOHN WILEY AND SONS, INC., 8^{th} edition, 2016. ISBN 9780470547557.

Roach, 1987. P.E. Roach. *The generation of nearly isotropic turbulence by means of grids*. International Journal of Heat and Fluid Flow, 8(2), 82 – 92, 1987. ISSN 0142-727X. doi: https://doi.org/10.1016/0142-727X(87)90001-4. URL `http://www.sciencedirect.com/science/article/pii/0142727X87900014`.

Shahsavari et al., 2012. Setareh Shahsavari, Andrew Desouza, Majid Bahrami and Erik Kjeang. *Thermal analysis of air-cooled PEM fuel cells*. International Journal of Hydrogen Energy, 37(23), 18261 – 18271, 2012. ISSN 0360-3199. doi: https://doi.org/10.1016/j.ijhydene.2012.09.075. URL `http://www.sciencedirect.com/science/article/pii/S0360319912021131`.

Torsten Berning and Shakhshir, 2018. Xin Gao Torsten Berning and Saher Al Shakhshir. *The effect of turbulence grid on the stack performance of an air-cooled proton exchange membrane fuel cell*, 2018.

Versteeg and Malalasekera, 2007. H K Versteeg and W Malalasekera. *An introduction to Computational Fluid Dynamics*. Pearson Education Limited, 2007. ISBN 978-0-13-127498-3.

Yin, 2016. Chungen Yin. *Near-wall modelling*, 2016.

Çengel, 2011. Yunus A. Çengel. *Fundamentals of Heat and Mass Transfer*. McGraw Hill, 3^{th} edition, 2011. ISBN 978-0071257398.